Search for *P*-odd Asymmetry of Prompt Neutron Emission in ^{235}U Fission Induced by Cold Polarized Neutrons¶

E. V. Brakhman[1], G. V. Danilyan[1], A. V. Fedorov[1], I. L. Karpikhin[†], V. A. Krakhotin[1], V. S. Pavlov[1], R. Golub[2], E. I. Korobkina[2], and T. Wilpert[2]

[1] *State Scientific Center of the Russian Federation Institute for Theoretical and Experimental Physics, Moscow, 117218 Russia*
e-mail: danilyan@itep.ru

[2] *Berlin Neutron Scattering Center of Hahn-Meitner Institute, D-14109 Berlin, Germany*

Received October 21, 2004

The preliminary result of the *P*-odd asymmetry of prompt neutron emission in ^{235}U fission induced by polarized cold neutrons is $a = (2.7 \pm 0.8) \times 10^{-5}$. Only scission neutrons can show such asymmetry, whereas neutrons emitted by excited fragments are the unavoidable background, which suppress the sought asymmetry. The *P*-odd asymmetry of light fragment emission for ^{235}U is equal to $(8.4 \pm 0.6) \times 10^{-5}$. Assuming that the last figure defines the parity mixture of the fissile nucleus, then the suppression factor is equal approximately to 3. © 2004 MAIK "Nauka/Interperiodica".

PACS numbers: 24.70.+s; 24.80.+y; 25.85.Ec

The problem of scission neutron existence remains one of the unsolved problems in fission physics. Scission neutrons are the neutrons emitted by a fissile nucleus before or during its rupture into two fragments. The angular distribution of these neutrons must differ from that for neutrons emitted from excited fragments completely accelerated by Coulomb force. The latter must be elongated with the fission axis due to summation of velocities. A common technique to search for scission neutrons is the fitting of angular and energy distributions of prompt fission neutrons by two components. The first one is the contribution of the fragment neutrons. The angular distribution of the second component is assumed to be approximately isotropic (scission neutrons). This technique gives very contradictory results. The fraction of the second component varies from 1 to 35% depending on the experiment and the assumptions made [1]. Thus, it is necessary to work out an alternative method to search for scission neutrons.

We suppose that the specific angular correlations such as left–right asymmetry of prompt fission neutron emission,

$$W = \mathrm{const}(1 + b\mathbf{n}_{\mathrm{pfn}}[\mathbf{n}_{\mathrm{in}}, \mathbf{S}]) \qquad (1)$$

or *P*-odd asymmetry of scission neutron emission,

$$W = \mathrm{const}(1 + a\mathbf{n}_{\mathrm{pfn}}, \mathbf{S}), \qquad (2)$$

where *b* and *a* are the asymmetry coefficients; $\mathbf{n}_{\mathrm{pfn}}$ and $\mathbf{n}_{\mathrm{in}}$ are the unit vectors in the direction of prompt fission neutron and initial neutron momenta, respectively; and **S** is the unit vector in the captured neutron spin direction, can be considered as evidence of scission neutron existence, because the same asymmetries for neutrons evaporated from fragments must be washed out due to summation of asymmetry coefficients over a huge number of final states in the fission process. Of course, the neutrons emitted by fragments can show the *P*-odd asymmetry reflecting the *P*-odd asymmetry in fragments, since light fragments emit 30% more neutrons than heavy ones. But the geometry of the experiment can be chosen to suppress this "kinematic" effect greatly.

It is obvious that this method is free of arbitrary assumptions.

Some time ago, we measured the left–right asymmetry of prompt neutron emission in fission of ^{235}U by polarized thermal neutrons, i.e., correlation (1). This asymmetry is the result of *s*- and *p*-wave interference in the entrance channel of the reaction. The magnitude of the left–right asymmetry coefficient for fission fragments is about 3×10^{-4}. The same coefficient for prompt neutrons measured at the angle $\theta = 90°$ between the detected neutron momentum and the fission axis was found to be equal to $b = (-5.8 \pm 1.4) \times 10^{-5}$ [2]. The difference must be caused by the asymmetry suppression due to the large background of fragment neutrons. It is easy to show that the factor of suppression is equal to

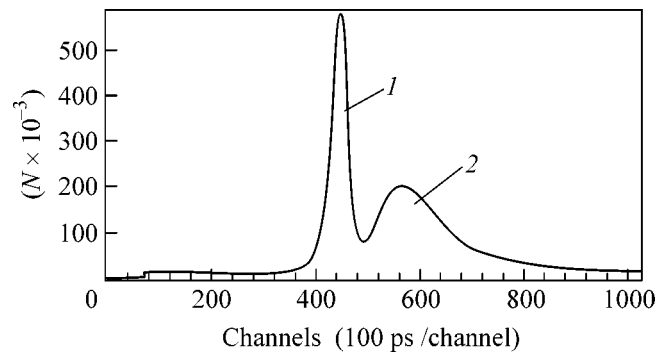$$\eta = 1 + N_{\mathrm{fr}}(\theta)/N_{\mathrm{sc}}. \qquad (3)$$

¶ This article was submitted by the authors in English.
† Deceased.

Fig. 2. (*1*) γ peak and (*2*) prompt fission neutron peak.
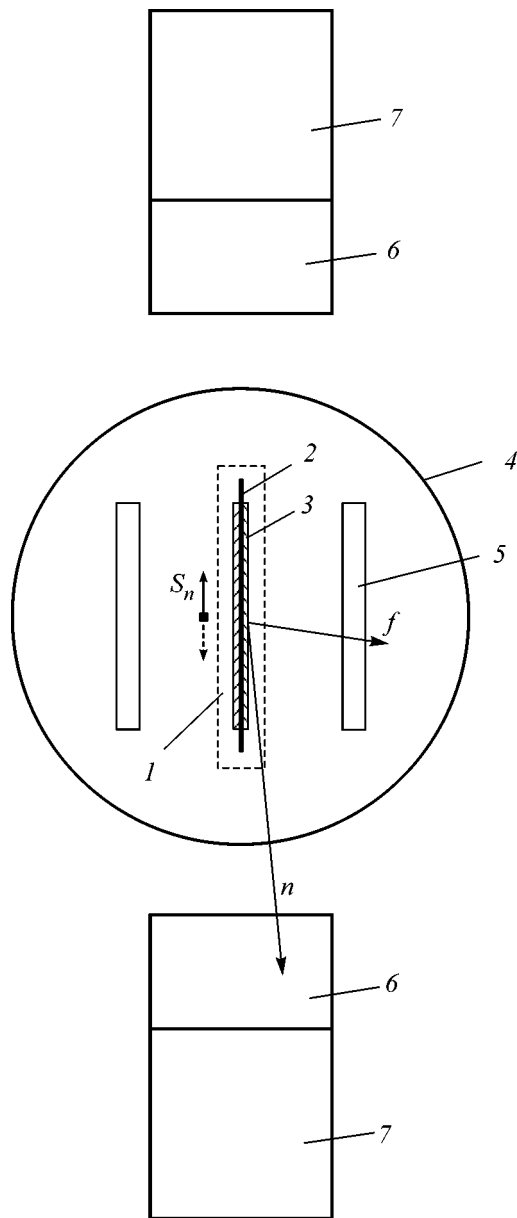
Fig. 1. Experimental setup: (*1*) cross section of *n* beam; (*2*) Zr plate; (*3*) U_3O_8 layers; (*4*) fission chamber; (*5*) fission fragment detectors; (*6*) scintillators; (*7*) photomultipliers.

This is a negative feature of the background in asymmetry measurements. But there is a positive one too. As was already pointed out, the angular distribution of fragment neutrons is elongated with the fission axis. Thus, the background and, therefore, the factor of asymmetry suppression depend on the angle between the momentum of detected prompt neutrons and the fission axis. The background is minimal at an angle of 90°, and it is maximal at 0°. So, the measurement at two angles (for example, at 90° and 45°) can give η, and, therefore, it is possible to evaluate the fraction of scission neutrons. The experiment [2] has been performed on the polarized thermal neutron beam of the MEPhI

small reactor, and the low intensity of the neutron beam does not permit us to measure with high accuracy correlation (1) at an angle of 45° to find the magnitude of η.

Nevertheless, to solve the problem, we have performed the measurements of correlation (2) on the polarized cold neutron beam of the reactor BER-II of BENSC HMI. For the first step, we searched for the *P*-odd asymmetry of prompt neutron emission in ^{235}U fission. The geometry of the experiment is shown in Fig. 1.

The setup consisted of a fission chamber, including target and fragment detectors, neutron detectors, electronic modules (CAMAC), and a computer. The target's size was 20×100 mm. It contained 24 mg of $^{235}U_3O_8$ placed on both sides of a thick Zr plate. Two multiwire low-pressure proportional counters were situated on both sides of the target to detect fission fragments. They did not distinguish between light and heavy fragments. The neutron beam was polarized in the plane of the target, perpendicularly to the direction of the beam and to the average direction of momentum of fission fragments. The polarization of the neutron beam was about 85%. The target and fragment detectors were enclosed in an aluminum chamber. The chamber was filled with isobutane up to a pressure of 10 Torr. Two neutron detectors were placed outside the chamber in orthogonal geometry to the beam direction and to the fission axis at a distance of 25 cm from the center of the target. These detectors consisted of a plastic scintillator and FEU-63 photomultiplier. To distinguish between prompt fission neutrons and prompt fission γ quanta, the time-of-flight technique was used. The pulses from the fragment detectors were triggers of the fission events and were used as start signals for the time-to-amplitude converters (TAC). The stop signals were the pulses from neutron detectors. The TAC signals were fed to the inputs of an ADC computer card. The four scalers were used in parallel to the TAC–ADC system. The polarization of the neutron beam was reversed by the signal from the experiment control module once per second. The data acquisition program collected spectra

Experimental results

	$A_n^* \times 10^5$	$A_\gamma^* \times 10^5$
Detector 1	$+3.5 \pm 1.1$	$+0.7 \pm 0.9$
Detector 2	$+1.9 \pm 1.1$	-0.9 ± 0.9
Average	$+2.7 \pm 0.8$	-0.1 ± 0.6

of the delayed coincidences and data from scalers for both directions of neutron beam polarization. It also showed the on-line results. The numbers of detected fission fragments and pulses from photomultipliers were monitored too. All runs were divided into 15-min exposures. We measured the value

$$A_n^* = (N^+ - N^-)/(N^+ + N^-). \qquad (4)$$

Here, N^+ and N^- are sum of the events under the neutron peak in the delayed coincidence spectrum (Fig. 2) for opposite directions of neutron beam polarization. The same value for the asymmetry of the coincidence under the gamma peak was also measured. The latter was used for checking the apparatus asymmetry. We also reversed the direction of the guiding magnetic field in the second half of the measurements. No apparatus asymmetry was found. The results for both neutron detectors are shown in the table.

The value of asymmetry measured at 90° relative to the fission axis lies in the interval

$$1.4 \times 10^{-5} \le A^* \le 4.0 \times 10^{-5} \text{ at } 90\% \text{ c.l.}$$

The experiment will be continued to measure the asymmetry at two angles (90° and 45°) with accuracy better than 4×10^{-6}.

REFERENCES

1. N. V. Kornilov, A. B. Kagalenko, and F.-J. Hambsch, Phys. At. Nucl. **64**, 1373 (2001).
2. G. V. Danilyan, V. A. Krakhotin, V. S. Pavlov, and A. V. Fedorov, JETP Lett. **76**, 697 (2002).

High Accuracy Description of Radiative Return Production of Low-Mass Muon and Pion Pairs at e^+e^- Colliders[¶]

A. B. Arbuzov[1], E. Bartoš[1], V. V. Bytev[1], E. A. Kuraev[1], and Z. K. Silagadze[2]

[1] *Joint Institute for Nuclear Research, Dubna, Moscow region, 141980 Russia*
e-mail: kuraev@thsun1.jinr.ru
[2] *Budker Institute of Nuclear Physics, Novosibirsk, 630090 Russia*
Received November 2, 2004

The process of muon (pion) pair production with small invariant mass in electron–positron high-energy annihilation, accompanied by emission of a hard photon at large angles, is considered. We find that the Drell–Yan picture for the differential cross section is valid in the charge-even experimental setup. Radiative corrections both for the electron block and for the final-state block are taken into account. © *2004 MAIK "Nauka/Interperiodica".*

PACS numbers: 11.80.La; 12.20.Ds; 13.66.–a

1. INTRODUCTION

The radiative return method, where the hard initial-state radiation is used to reduce the invariant mass of a hadronic system produced in high-energy electron–positron annihilation, provides an important tool to study various hadronic cross sections in a wide range of invariant masses without actually changing the center-off-mass energy of the collider [1]. The very high luminosity of the modern meson factories makes the method competitive with the more conventional energy scan approach [2, 3]. Preliminary experimental studies at KLOE [4], BABAR [5], and BELLE confirm the excellent potential of the radiative return method. The case of resonance production by this mechanism was first considered in [6]. Recently, considerable efforts were devoted to elucidate the theoretical understanding of the radiative return process, especially for the case of low-energy pion pair production (see, for example, [7, 8]). Here, by means of explicit calculations, we confirm the Drell–Yan form of the cross section. This fact allows us to take into account all leading and next-to-leading terms in all orders of perturbation theory (PT) and as a consequence to improve the accuracy of theoretical predictions.

The case where the invariant mass of the hadron system $\sqrt{s_1}$ is small compared to the center-of-mass total energy $\sqrt{s} = 2\varepsilon$ represents a special interest. Such a situation is realized, for example, in the BABAR radiative return studies, where such interesting physical quantities as form factors of the pion and the nucleon can be investigated. The processes of radiative annihilation into muon and pion pairs considered here play a crucial role in such studies, both for normalization purposes

and as one of the main hadron production process at low energies. A description of their differential cross sections with a rather high level of accuracy (better than 0.5% in the muon case) at the energies of BABAR experiment is the goal of our paper. The high accuracy of theoretical calculations in the framework of QED becomes very significant in precise measurement of the strong interaction effects in $g - 2$ muon (KLOE), and this is one of the motivations of our paper.

We specify the kinematics of the radiative muon (pion) pair creation process

$$e_-(p_-) + e_+(p_+) \longrightarrow \mu_-(q_-) + \mu_+(q_+) + \gamma(k_1), \quad (1)$$

as follows:

$$p_\pm^2 = m^2, \quad q_\pm^2 = M^2, \quad k_1^2 = 0,$$

$$\chi_\pm = 2k_1 p_\pm, \quad \chi'_\pm = 2k_1 q_\pm, \quad s = (p_- + p_+)^2,$$

$$s_1 = (q_- + q_+)^2, \quad t = -2p_- q_-, \quad t_1 = -2p_+ q_+, \quad (2)$$

$$u = -2p_- q_+, \quad u_1 = -2p_+ q_-,$$

where m and M are the electron and muon (pion) masses, respectively. Throughout the paper, we will assume

$$s \sim -t \sim -t_1 \sim -u \sim -u_1 \gg 4M^2 \gg m^2, \quad (3)$$

and $s \gg s_1 > M^2$.

We will systematically omit the terms of order M^2/s and m^2/s_1 compared with the leading ones. In $\mathbb{O}(\alpha)$ radiative corrections, we will also drop terms suppressed by the factor s_1/s. Also, we imply that the invariant mass $s_1 \ll M_Z^2$, where M_Z is the mass of the Z boson (due to which we do not consider the weak interactions).

___
[¶] This article was submitted by the authors in English.

In this paper, we will consider only the charge-even part of the differential cross section, which can be measured in an experimental setup blind to the charges of the created particles. So we omit the contribution from a box-type FD when an additional virtual photon connects both the muon and the electron line. In the final state, we consider corrections only in the lowest order of PT including one-loop virtual corrections, soft real ones, and hard real photon contributions. We imply that the invariant mass of the final pairs with photon emission is small compared with $\sqrt{s}$.

Our paper is organized as follows. The next section is devoted to the Born level cross section. Radiative corrections to the final and initial states are considered in Section 3. The main result of the paper is found in Section 3.3. This is followed by concluding remarks.

2. THE BORN LEVEL CROSS SECTION

Within the Born approximation, the corresponding contribution to the cross section is

$$\frac{d\sigma_B^j}{d\Gamma} = \frac{\alpha^3}{8\pi^2 s s_1^2} R^j, \quad R^j = B^{\rho\sigma} i_{\rho\sigma}^{(0j)}, \quad j = \mu, \pi, \quad (4)$$

$$B_{\rho\sigma} = B_g g_{\rho\sigma} + B_{11}(p_- p_-)_{\rho\sigma} + B_{22}(p_+ p_+)_{\rho\sigma},$$

$$B_g = -\frac{(s_1 + \chi_+)^2 + (s_1 + \chi_-)^2}{\chi_+ \chi_-}, \quad (5)$$

$$B_{11} = -\frac{4s_1}{\chi_+ \chi_-}, \quad B_{22} = -\frac{4s_1}{\chi_+ \chi_-},$$

where we have used the shorthand notation $(qq)_{\rho\sigma} = q_\rho q_\sigma$, $(pq)_{\rho\sigma} = p_\rho q_\sigma + q_\rho p_\sigma$. For the muon final state,

$$i_{\rho\sigma}^{(0\mu)} = 4\left[(q_+ q_-)_{\rho\sigma} - g_{\rho\sigma}\frac{s_1}{2}\right]. \quad (6)$$

For the case of pions,

$$i_{\rho\sigma}^{(0\pi)} = \left|F_\pi^{str}(s_1)\right|^2 (q_- - q_+)_\rho (q_- - q_+)_\sigma, \quad (7)$$

where $F_\pi^{str}(s_1)$ is the pion strong interaction form factor, in which we include the all effects of strong interactions in two-pion formation.

Note that the Born level cross section for the $e^+ e^- \longrightarrow \mu^+ \mu^- \gamma$ process was calculated in [9].

For the case of small invariant mass of the created pair $s_1 \ll s$, the phase space volume of the final particles can be rewritten as

$$d\Gamma = \pi^2 dx_- dc ds_1, \quad (8)$$

(note that s_1 is small due to $c \longrightarrow 1$, but the energy of muon pair is large: $s x_\pm^2 \gg 4M^2$) and approximately

$$x_\pm = \varepsilon_\pm / \varepsilon, \quad x_+ + x_- = 1,$$
$$c = \cos(\widehat{\mathbf{p}_- \mathbf{q}_-}) = \cos\theta. \quad (9)$$

We will assume that the emission angle of the hard photon lies outside the narrow cones around the beam axis: $\theta_0 < \theta_1 < \pi - \theta_0$, with $\theta_0 \ll 1$, $\theta_0 \varepsilon \gg M$.

When the initial-state radiation dominates, the Born cross section takes a rather simple form:

$$d\sigma_B^{(\mu)}(p_-, p_+; k_1, q_-, q_+)$$

$$= \frac{\alpha^3 (1 + c^2)}{s s_1 (1 - c^2)} [2\sigma + 1 - 2x_- x_+] dx_- dc ds_1,$$

$$d\sigma_B^{(\pi)}(p_-, p_+; k_1, q_-, q_+) \quad (10)$$

$$= \frac{\alpha^3 (1 + c^2)}{s s_1 (1 - c^2)} \left|F_\pi^{str}(s_1)\right|^2 [-\sigma + x_- x_+] dx_- dc ds_1,$$

$$\frac{1}{2}(1 - \beta) < x_- < \frac{1}{2}(1 + \beta), \quad \beta = \sqrt{1 - \frac{4M^2}{s_1}}, \quad \sigma = \frac{M^2}{s_1}.$$

Here, β is the velocity of the pair component in the center-of-mass reference frame of the pair.

3. RADIATIVE CORRECTIONS

Radiative corrections (RC) can be separated into three gauge-invariant parts. They can be taken into account by the formal replacement (see (4))

$$\frac{R^j}{s_1^2} \longrightarrow \frac{K^{\rho\sigma} J_{\rho\sigma}^j}{s_1^2 |1 - \Pi(s_1)|^2} \quad (11)$$

where $\Pi(s_1)$ describes the vacuum polarization of the virtual photon, $K^{\rho\sigma}$ is the initial-state emission Compton tensor with RC taken into account, and $J_{\rho\sigma}^j$ is the final-state current tensor with $\mathbb{O}(\alpha)$ RC.

First, we consider the explicit formulas for RC due to virtual, soft, and hard collinear final state emission. As concerning RC to the initial state for the charge-blind experimental setup considered here, we will use the explicit expression for the Compton tensor with heavy photon $K^{\rho\sigma}$ calculated in [10] for the scattering channel and apply the crossing transformation. A possible contribution due to emission of an additional real photon from the initial state will be taken into account too.

3.1. Corrections to the Final State

The third part is related to the lowest order RC to the muon (pion) current [11]

$$J_{\rho\sigma} = i_{\rho\sigma}^{(v)} + i_{\rho\sigma}^{(s)} + i_{\rho\sigma}^{(h)}. \qquad (12)$$

The virtual photon contribution $i_{\rho\sigma}^{(v)}$ takes into account the Dirac and Pauli form factors of the muon current

$$B^{\rho\sigma}i_{\rho\sigma}^{(v\mu)} = B_g \sum_{\text{pol}} |J_\rho^{(v\mu)}|^2$$

$$+ B_{11}\left[\sum_{\text{pol}} |p_- J^{(v\mu)}|^2 + \sum_{\text{pol}} |p_+ J^{(v\mu)}|^2\right]. \qquad (13)$$

Here, Σ means a sum over the muon spin states and

$$\sum_{\text{pol}} |J_\rho^{(v\mu)}|^2 = \frac{\alpha}{\pi}[-8(s_1 + 2M^2)f_1^{(\mu)} - 12s_1 f_2^{(\mu)}],$$

$$\sum_{\text{pol}} |J^{(v\mu)}p_\pm|^2 = \frac{\alpha}{\pi}s^2(1 \pm c)^2\left(x_+ x_- f_1^{(\mu)} + \frac{1}{4}f_2^{(\mu)}\right). \qquad (14)$$

For the pion final state, we have

$$B^{\rho\sigma}i_{\rho\sigma}^{(v\pi)} = 2\frac{\alpha}{\pi}B^{\rho\sigma}i_{\rho\sigma}^{(0\pi)}f_\pi^{QED},$$

$$B^{\rho\sigma}i_{\rho\sigma}^{(0\pi)} = 2\frac{\alpha}{\pi}|F_\pi^{str}(s_1)|^2$$

$$\times \left[(4M^2 - s_1)B_g + \frac{1}{8}s^2 B_{11}(x_+ - x_-)^2(1 + c^2)\right]f_\pi^{QED}.$$

The explicit expression for the $f_{1,2}^\mu$, f_π^{QED} form factors of the pion and muon are well known [11].

The soft photon correction to the final-state currents reads

$$i_{\rho\sigma}^{(s\pi)} = \frac{\alpha}{\pi}\Delta_{1'2'}i_{\rho\sigma}^{(0\pi)}, \quad i_{\rho\sigma}^{(s\mu)} = \frac{\alpha}{\pi}\Delta_{1'2'}i_{\rho\sigma}^{(0\mu)},$$

$$\Delta_{1'2'} = -\frac{1}{4\pi}\int\frac{d^3k}{\omega}\left(\frac{q_+}{q_+k} - \frac{q_-}{q_-k}\right)^2\Bigg|_{w \leq \Delta_\varepsilon}$$

$$= \left(\frac{1 + \beta^2}{2\beta}\ln\frac{1 + \beta}{1 - \beta} - 1\right)\ln\frac{(\Delta\varepsilon)^2 M^2}{\varepsilon^2 x_+ x_- \lambda^2}$$

$$+ \frac{1 + \beta^2}{2\beta}\left[-g - \frac{1}{2}\ln^2\frac{1 + \beta}{1 - \beta}\right.$$

$$- \ln\frac{1 + \beta}{1 - \beta}\ln\frac{1 - \beta^2}{4} - \frac{\pi^2}{6} - 2\text{Li}_2\left(\frac{\beta - 1}{\beta + 1}\right)\Bigg],$$

$$g = 2\beta\int_0^1\frac{dt}{1 - \beta^2 t^2}\ln\left(1 + \frac{1 - t^2}{4}\frac{(x_+ - x_-)^2}{x_+ x_-}\right)$$

$$= \ln\left(\frac{1 + \beta}{1 - \beta}\right)\ln(1 + z - z/\beta^2)$$

$$+ \text{Li}_2\left(\frac{1 - \beta}{1 + \beta/r}\right) + \text{Li}_2\left(\frac{1 - \beta}{1 - \beta/r}\right)$$

$$- \text{Li}_2\left(\frac{1 + \beta}{1 - \beta/r}\right) - \text{Li}_2\left(\frac{1 + \beta}{1 + \beta/r}\right),$$

$$\beta = \sqrt{1 - \frac{4M^2}{s_1}}, \quad z = \frac{1}{4}\left(\sqrt{\frac{x_+}{x_-}} - \sqrt{\frac{x_-}{x_+}}\right)^2,$$

$$r = |x_+ - x_-|.$$

These formulas provide the generalization of the known expression (see (25), (26) in [12]) for the case of small invariant mass $4M^2 \sim \sqrt{s_1} \ll \varepsilon_\pm$.

The contribution of an additional hard photon emission (with momentum k_2) by the muon block, provided $\tilde{s}_1 = (q_+ + q_- + k_2)^2 \sim s_1 \ll s$, can be found by the expression

$$B^{\rho\sigma}i_{\rho\sigma}^{(h\mu)} = \frac{\alpha}{4\pi^2}\int\frac{d^3k_2}{\omega_2}B^{\rho\sigma}\sum J_\rho^{(\gamma)}(J_\sigma^{(\gamma)})^*\Bigg|_{\omega_2 \geq \Delta\varepsilon}, \quad (15)$$

with

$$\sum |J_\rho^{(\gamma)}|^2 = 4Q^2(s_1 + 2k_2 q_- + 2k_2 q_+ + 2M^2)$$

$$- 8\frac{(k_2 q_-)^2 + (k_2 q_+)^2}{(k_2 q_-)(k_2 q_+)}, \quad Q = \frac{q_-}{q_- k_2} - \frac{q_+}{q_+ k_2},$$

and

$$\sum |J^{(\gamma)}p_\pm|^2 = -8Q^2(q_- p_\pm)(q_+ p_\pm)$$

$$+ 8(p_\pm k_2)\left(Qq_+\frac{p_\pm q_-}{q_+ k_2} - Qq_-\frac{p_\pm q_+}{q_- k_2}\right)$$

$$+ 8(p_\pm k_2)\left(\frac{p_\pm q_-}{q_+ k_2} + \frac{p_\pm q_+}{q_- k_2}\right) \qquad (16)$$

$$+ 8(p_\pm Q)(p_\pm q_+ - p_\pm q_-) - 8\frac{(k_2 p_\pm)^2 M^2}{(k_2 q_+)(k_2 q_-)}.$$

For the case of charged pion pair production, the radiative current tensor has the form

$$i_{\rho\sigma}^{(h\pi)} = -\frac{\alpha}{4\pi^2}\int|F_\pi^{str}(\tilde{s}_1)|^2\frac{d^3k_2}{\omega_2}\left[\frac{M^2}{\chi_{2-}^2}(Q_1 Q_1)_{\rho\sigma}\right.$$

$$+ \frac{M^2}{\chi_{2+}^2}(Q_2 Q_2)_{\rho\sigma} - \frac{q_+ q_-}{\chi_{2+}\chi_{2-}}(Q_1 Q_2)_{\rho\sigma}$$

$$+ g_{\rho\sigma} - \frac{1}{\chi_{2-}}(Q_1 q_-)_{\rho\sigma} + \frac{1}{\chi_{2+}}(Q_2 q_+)_{\rho\sigma}\Bigg]\Bigg|_{\omega_2 > \Delta\varepsilon}, \quad (17)$$

$$Q_1 = q_- - q_+ + k_2, \quad Q_2 = q_- - q_+ - k_2,$$

$$\chi_{2\pm} = 2k_2 q_\pm.$$

One can check that the Bose symmetry and the gauge invariance condition are valid for the pionic current tensor. Namely, it is invariant with regard to the permutation of the pion momenta and goes to zero after conversion with 4-vector q.

The sum of soft and hard photon corrections to the final current does not depend on $\Delta\varepsilon/\varepsilon$.

3.2. Corrections to the Initial State

Let us now consider the Compton tensor with RC, which describe virtual corrections to the initial state. In our kinematical region, it will be convenient to rewrite the tensor explicitly extracting large logarithms. We will distinguish two kinds of large logarithms:

$$l_s = \ln\frac{s}{m^2}, \quad l_1 = \ln\frac{s}{s_1}. \quad (18)$$

We rewrite the Compton tensor [10] in the form

$$K_{\rho\sigma} = \left(1 + \frac{\alpha}{2\pi}\rho\right)B_{\rho\sigma} + \frac{\alpha}{2\pi}\Bigg[\tau_g g_{\rho\sigma} + \tau_{11}(p_-p_-)_{\rho\sigma}$$

$$+ \tau_{22}(p_+p_+)_{\rho\sigma} - \frac{1}{2}\tau_{12}(p_-p_+)_{\rho\sigma}\Bigg], \quad (19)$$

$$\rho = -4\ln\frac{m}{\lambda}(l_s - 1) - l_s^2 + 3l_s - 3l_1 + \frac{4}{3}\pi^2 - \frac{9}{2},$$

with τ_i given in [10].

The infrared singularity (the presence of the *photon mass* λ in ρ) is compensated by taking into account soft photon emission from the initial particles:

$$d\sigma^{\text{soft}} = d\sigma_0 \frac{\alpha}{\pi}\Delta_{12},$$

$$\Delta_{12} = -\frac{1}{4\pi}\int\frac{d^3k}{\omega}\left(\frac{p_+}{p_+k} - \frac{p_-}{p_-k}\right)^2\Bigg|_{\omega \leq \Delta\varepsilon} \quad (20)$$

$$= 2(l_s - 1)\ln\frac{m\Delta\varepsilon}{\lambda\varepsilon} + \frac{1}{2}l_s^2 - \frac{\pi^2}{3}.$$

As a result, the quantity ρ in formula (19) will change to

$$\rho \longrightarrow \rho_\Delta = \left(4\ln\frac{\Delta\varepsilon}{\varepsilon} + 3\right)(l_s - 1) - 3l_1 + \frac{2\pi^2}{3} - \frac{3}{2}.$$

The cross section of two-hard-photon emission for the case when one of them is emitted collinearly to the

incoming electron or positron can be obtained by means of the quasi-real electron method [13]:

$$\frac{d\sigma^j_{\gamma\gamma,\,\text{coll}}}{dx_- dc ds_1} = dW_{p_-}(k_3)\frac{d\tilde\sigma^j_B(p_-(1-x_3), p_+; k_1, q_+, q_-)}{dx_- dc ds_1}$$

$$+ dW_{p_+}(k_3)\frac{d\tilde\sigma^j_B(p_-, p_+(1-x_3); k_1, q_+, q_-)}{dx_- dc ds_1},$$

with

$$dW_p(k_3) = \frac{\alpha}{\pi}\left[\left(1 - x_3 + \frac{x_3^2}{2}\right)\ln\frac{(\varepsilon\theta_0)^2}{m^2} - (1 - x_3)\right]\frac{dx_3}{x_3},$$

$$x_3 = \frac{\omega_3}{\varepsilon}, \quad x_3 > \frac{\Delta\varepsilon}{\varepsilon}.$$

Here, we suppose that the polar angle θ_3 between the directions of the additional collinear photon and the beam axis does not exceed some small value $\theta_0 \ll 1$, $\varepsilon\theta_0 \gg m$.

The *boosted* differential cross section $d\tilde\sigma^j_B(p_-x, p_+y; k_1, q_+, q_-)$ with reduced momenta of the incoming particles reads (compare with Eq. (10))

$$\frac{d\tilde\sigma^\mu_B(p_+x_2, p_-x_1; k_1, q_+, q_-)}{dx_- dc ds_1}$$

$$= \frac{\alpha^3(1 + 2\sigma - 2\nu_-(1 - \nu_-))(x_1^2(1-c)^2 + x_2^2(1+c)^2)}{s_1 s x_1^2 x_2^2(1-c^2)(x_1 + x_2 + c(x_2 - x_1))}, \quad (21)$$

$$\frac{d\tilde\sigma^\pi_B(p_+x_2, p_-x_1; k_1, q_+, q_-)}{dx_- dc ds_1}$$

$$= \frac{\alpha^3(\nu_-(1 - \nu_-) - \sigma)(x_1^2(1-c)^2 + x_2^2(1+c)^2)}{s_1 s x_1^2 x_2^2(1-c^2)(x_1 + x_2 + c(x_2 - x_1))},$$

$$\nu_- = \frac{x_-}{y_2}, \quad y_2 = \frac{2x_1 x_2}{x_1 + x_2 + c(x_2 - x_1)}. \quad (22)$$

In a certain experimental situation, an estimate of the contribution of the additional hard photon emission outside the narrow cones around the beam axes is needed. It can be estimated by

$$\frac{d\sigma^j_{\gamma\gamma,\,\text{noncoll}}}{dx_- dc ds_1} = \frac{\alpha}{4\pi^2}\int\frac{d^3k_3}{\omega_3}\left[\frac{\varepsilon^2 + (\varepsilon - \omega_3)^2}{\varepsilon\omega_3}\right]$$

$$\times \Bigg\{\frac{1}{k_3 p_-}\frac{d\sigma^j_B(p_-(1-x_3), p_+; k_1, q_+, q_-)}{dx_- dc ds_1}$$

$$+ \frac{1}{k_3 p_+}\frac{d\sigma^j_B(p_-, p_+(1-x_3); k_1, q_+, q_-)}{dx_- dc ds_1}\Bigg\},$$

$$x_3 = \omega_3/\varepsilon,$$

where the integration was done under the condition that $\theta_3 \geq \theta_0$, $\Delta\varepsilon < \omega_3 < \omega_1$.

It is a simplified expression for the two-photon initial-state emission cross section. The deviation of our estimate from the exact result for the case of a large-angle emission is small. It does not depend on s and depends slightly on θ_0. For $\theta_0 \sim 10^{-2}$, we have

$$\frac{\pi}{\alpha}\left|\frac{\int(d\sigma^j_{\gamma\gamma,\,\text{noncoll}} - d\sigma^j_{\gamma\gamma,\,\text{noncoll exact}})}{\int d\sigma^j_B}\right| \lesssim 10^{-1}. \qquad (23)$$

3.3. Master Formula

By summing up all contributions for the charge-even part, we can put the cross section of the radiative production in the form

$$\frac{d\sigma^j(p_+, p_-; k_1, q_+, q_-)}{dx_-dcds_1}$$

$$= \int\limits_{}^{1}\int\limits_{}^{1}\frac{dx_1 dx_2}{|1 - \Pi(sx_1x_2)|^2}\frac{d\tilde\sigma^j_B(p_+x_2, p_-x_1; k_1, q_+, q_-)}{dx_-dcds_1}$$

$$\times D(x_1, l_s)D(x_2, l_s)\left(1 + \frac{\alpha}{\pi}K^j\right)$$

$$+ \frac{\alpha}{2\pi}\int\limits_{\Delta}^{1}dx\left[\frac{1 + (1-x)^2}{x}\ln\frac{\theta_0^2}{4} + x\right] \qquad (24)$$

$$\times\left[\frac{d\tilde\sigma^j_B(p_-(1-x), p_+; k_1, q_+, q_-)}{dx_-dcds_1}\right.$$

$$+ \left.\frac{d\tilde\sigma^j_B(p_-, p_+(1-x); k_1, q_+, q_-)}{dx_-dcds_1}\right] + \frac{d\sigma^j_{\gamma\gamma,\,\text{noncoll}}}{dx_-dcds_1},$$

$$D(x, l_s) = \delta(1-x) + \frac{\alpha}{2\pi}P^{(1)}(x)(l_s - 1) + \dots,$$

$$\Delta = \frac{\Delta\varepsilon}{\varepsilon}, \quad P^{(1)}(x) = \left(\frac{1+x^2}{1-x}\right)_+, \quad j = \mu, \pi.$$

The boosted cross section $d\tilde\sigma$ is defined above in Eq. (21). The lower limits of the integrals over $x_{1,2}$ depend on the experimental conditions.

The structure function D includes all dependence on the large logarithm l_s. The so-called K factor reads

$$K^j = \frac{1}{R^j}B^{\lambda\sigma}(i^{(vj)}_{\lambda\sigma} + i^{(sj)}_{\lambda\sigma} + i^{(hj)}_{\lambda\sigma}) + R^{(j)}_{\text{compt}}. \qquad (25)$$

Quantities $R^{(j)}_{\text{compt}}$ include the "nonleading" contributions from the initial-state radiation. Generally, they

are rather cumbersome expressions for the case $s_1 \sim s$. For the case $s_1 \sim M^2 \ll s$, we obtain

$$R^{(\mu)}_{\text{compt}} = R^{(\pi)}_{\text{compt}} + \frac{c^2}{(1 - 2x_-x_+ + 2\sigma)(1 + c^2)},$$

$$R^{(\pi)}_{\text{compt}} = \frac{1 - c^2}{4(1 + c^2)}\left\{\frac{5 + 2c + c^2}{1 - c^2}\ln^2\left(\frac{2}{1+c}\right)\right.$$

$$- \frac{5-c}{1+c}\ln\left(\frac{2}{1+c}\right) + \frac{5 - 2c + c^2}{1 - c^2}\ln^2\left(\frac{2}{1-c}\right) \qquad (26)$$

$$\left. - \frac{5+c}{1-c}\ln\left(\frac{2}{1-c}\right) - 4\frac{c^2}{1 - c^2}\right\} + \frac{\pi^2}{3}.$$

Here, we see remarkable phenomena: the cancellation of terms containing $\ln(s/s_1)$. In such a way, only one kind of large logarithm $\ln(s/m^2)$ enters into the final result. This fact is the consequence of the renormalization group invariance.

4. CONCLUSIONS

We have considered radiative muon (pion) pair production in high-energy electron–positron annihilation for a charge-blind experimental setup. In any event, the charge-odd part of the cross section under consideration is suppressed by the factor $s_1/s \ll 1$ in the kinematics discussed here.

Using the heavy-photon Compton tensor [10], we have calculated radiative corrections to this process. Although analogous calculations were performed earlier (see, for example, [8]), our main result, Eq. (24), is new. This result shows that the cross section in our quasi $2 \longrightarrow 2$ kinematics can be written in the form of the cross section of the Drell–Yan process. Thus, the results of [14] for the RC to the one-photon e^+e^- annihilation into hadrons are generalized to the situation where a hard photon at a large angle is present in the final state.

This generalization is not a trivial fact because of the two types of large logarithms present in the problem.

Possible background from the peripheral process $e\bar{e} \longrightarrow e\bar{e}\mu\bar{\mu}$ is negligible in our kinematics: it is suppressed by the factor $\frac{\alpha}{\pi}\frac{s_1}{s}$ and, moreover, can be eliminated if detection of the primary hard photon (see Eq. (1)) is required by the experimental cuts for event selection.

REFERENCES

1. V. N. Baier and V. A. Khoze, Zh. Éksp. Teor. Fiz. **48**, 946 (1965) [Sov. Phys. JETP **21**, 629 (1965)]; Yad. Fiz. **2**, 287 (1965) [Sov. J. Nucl. Phys. **2**, 205 (1966)]; M. S. Chen and P. M. Zerwas, Phys. Rev. D **11**, 58 (1975).

2. M. Benayoun, S. I. Eidelman, V. N. Ivanchenko, and Z. K. Silagadze, Mod. Phys. Lett. A **14**, 2605 (1999).

3. X. C. Lou, T. Benninger, and W. M. Dunwoodie, Nucl. Phys. A **675**, 253 (2000).

4. A. G. Denig *et al.* (KLOE Collab.), Nucl. Phys. (Proc. Suppl.) **116**, 243 (2003).

5. E. P. Solodov *et al.* (BABAR Collab.), in *Proceedings of the e^+e^- Physics at Intermediate Energies Conference*, Ed. by Diego Bettoni, eConf **C010430**, T03 (2001); hep-ex/0107027.

6. V. N. Baier and V. S. Fadin, Phys. Lett. B **27B**, 223 (1968).

7. H. Czyz, A. Grzelinska, J. H. Kuhn, and G. Rodrigo, Eur. Phys. J. C **27**, 563 (2003).

8. V. A. Khoze *et al.*, Eur. Phys. J. C **18**, 481 (2001); **25**, 199 (2002).

9. F. A. Berends and R. Kleiss, Nucl. Phys. B **177**, 237 (1981); E. A. Kuraev and G. V. Meledin, Nucl. Phys. B **122**, 485 (1977).

10. E. A. Kuraev, N. P. Merenkov, and V. S. Fadin, Yad. Fiz. **45**, 782 (1987) [Sov. J. Nucl. Phys. **45**, 486 (1987)].

11. A. I. Akhiezer and V. B. Berestetskiĭ, *Quantum Electrodynamics*, 4th ed. (Nauka, Moscow, 1981; Wiley, New York, 1965).

12. A. Arbuzov *et al.*, JETP **88**, 213 (1999).

13. P. Kessler, Nuovo Cimento **17**, 809 (1960); V. N. Baier, V. S. Fadin, and V. A. Khoze, Nucl. Phys. B **65**, 381 (1973); V. N. Baier, E. A. Kuraev, V. S. Fadin, and V. A. Khoze, Phys. Rep. **78**, 293 (1981).

14. E. A. Kuraev and V. S. Fadin, Sov. J. Nucl. Phys. **41**, 466 (1985); O. Nicrosini and L. Trentadue, Phys. Lett. B **196**, 551 (1987).

Internal Segregation of Nanoparticles Irradiated by Laser Radiation

V. V. Voronov[1], P. V. Kazakevich[2], A. V. Simakin[2], and G. A. Shafeev[2]

[1] *Laser Materials and Technologies Center, General Physics Institute, Russian Academy of Sciences, Moscow, 119991 Russia*
[2] *Wave Research Center, General Physics Institute, Russian Academy of Sciences, Moscow, 119991 Russia*
e-mail: shafeev@kapella.gpi.ru
Received November 1, 2004

The effect of the removal of zinc from brass nanoparticles has been experimentally discovered upon irradiating their suspension in ethanol by laser radiation. The analysis of the absorption spectra of nanoparticles shows that brass nanoparticles are transformed to copper nanoparticles during irradiation. The results are interpreted in terms of the high-pressure-induced modification of the phase diagram of nanoparticles. This pressure is caused by, first, the small radius of nanoparticles and, second, the pressure of the surrounding-liquid vapors upon the laser heating of nanoparticles. © 2004 MAIK "Nauka/Interperiodica".

PACS numbers: 42.62.–b; 61.46.+w; 78.66.–w

The selectivity of processes occurring upon the laser irradiation of electrolyte solutions is caused by the absorption of laser radiation by a certain type of aquaions in a solution [1]. The initial spatial distribution of ions in the solution is uniform, and the density of absorbing ions varies due to the thermal-diffusion-induced positive feedback between the laser-radiation intensity in the medium and density. Microparticles whose size is comparable with the wavelength of electromagnetic radiation can be efficiently accelerated by laser radiation due to the asymmetry of a vapor cloud arising upon their heating by a laser [2]. In contrast to laser ablation in vacuum, nanoparticles formed remain in the liquid and can again hit the laser beam, interacting with it. Nanoparticles are thermally thin up to the shortest duration of laser radiation pulses. Therefore, the liquid vapor surrounding a nanoparticle heated by laser radiation expands on all sides of it. Nanoparticles in liquids (so-called colloidal solutions) are a substantially heterogeneous medium. Under typical conditions, the mean distance between nanoparticles in a liquid (~1000 nm) is much larger than their size (~10 nm). In practically interesting cases, the liquid itself is transparent at the laser wavelength (i.e., its ions or molecules have no absorption bands in this region). Laser radiation is absorbed by nanoparticles due either to interband absorption—for superconducting particles—or to the plasma resonance of free current curriers—for metal nanoparticles. In the latter case, the position of the plasma-resonance peak depends on the kind of metal, the index of refraction of the surrounding medium, and (to a smaller degree) the nanoparticle size.

In a laser beam of moderate peak intensity (~10^9 W/cm^2), nanoparticles can be heated to the melt-ing temperature [3–7]. Energy absorbed from the laser beam is transferred to the surrounding liquid due to heat conduction, so that the nanoparticle is surrounded by a rapidly expanding vapor shell during the laser pulse and some time after it. The vapor pressure in the shell at the initial stage of its expansion is close to the pressure of the saturated vapors of the liquid at the melting temperature of the nanoparticle material, i.e., about 10^3 K for such metals as Au, Ag, and Cu. The interaction between the melted nanoparticle with the high-pressure vapors of the liquid can lead to the fragmentation of nanoparticles, for example, due to the asymmetry of the vapor cloud, and, finally, to a change in the size distribution function of nanoparticles [4]. The interaction between the ensemble of nanoparticles and the laser beam is also characterized by the presence of feedbacks. In particular, the generation of the second harmonic of radiation from a femtosecond titanium–sapphire laser on silver nanoparticles leads to a catastrophic decrease in their mean size from 15–20 to 1–2 nm due to the coincidence of the harmonic radiation with the plasma resonance of the nanoparticles [8]. The effective absorption cross section of nanoparticles at the laser wavelength depends on the detuning of this wavelength from the plasma-resonance peak. The melting of nanoparticles in the laser beam makes it possible to alloy them with nanoparticles of other metals that are present in the solution and have a smaller absorption cross section, for example, upon the laser irradiation of a mixture of Au and Ag nanoparticles [9].

In this paper, we report data on a new effect that is manifested upon the laser irradiation of nanoparticles of a metal alloy in a liquid. This effect is the removal of a component with lower melting temperature from a

nanoparticle, i.e., the purification of nanoparticles from impurities upon pulsed laser heating.

The material of the nanoparticle is subjected to additional pressure due to its small radius. In particular, due to this factor, the melting temperature of nanoparticles is lower than the value for the bulk material [10, 11]. For a liquid-copper nanoparticle, the Laplace pressure given by the expression $p = 2\sigma/r$, where σ is the surface tension coefficient and r is the particle radius, is equal to 120 MPa for $r = 20$ nm [12]. In addition to this pressure, the nanoparticle during the laser pulse is subjected to the vapor pressure of the surrounding liquid, which reaches a maximum simultaneously with the particle temperature and decreases rapidly upon expansion of the vapor shell. The pressure of ethanol vapors surrounding the particle with a temperature of 1500 K is estimated at about 20 MPa from the equation of state of the real gas. Note that the pressure of nanoparticle-substance vapors at the melting temperature for most metals is negligibly low compared to the above values. For high pressures, the phase diagram of the alloy either is noticeably deformed such that it is shifted toward the larger content of components with higher melting temperatures at the same alloy temperature or completely changes its shape [13]. The component with the lower melting temperature predominantly leaves the nanoparticle, and its composition changes. In a certain temperature interval, this component can be in the liquid state, while the more refractory component of the alloy still remains solid. Such an effect is considered in this work by example of brass nanoparticles consisting of 40% Zn and 60% Cu undergoing pulsed laser heating.

Brass and copper nanoparticles were obtained in the form of stable suspensions by the ablation of the respective metal targets in ethanol by pulsed radiation from either a copper-vapor laser (wavelength 0.51 μm and pulse duration 20 ns) or a Nd:YAG laser (wavelength 1.06 μm and pulse duration 130 ns). Immediately after preparation, copper nanoparticles exhibit a pronounced plasma resonance in the visible spectrum with a peak lying in the interval 570–590 nm [14]. Then, they are oxidized to copper oxide by air oxygen dissolved in the liquid, which results in the disappearance of the plasma resonance peak. In contrast, brass nanoparticles are stable to oxidation for at least several months. The position of the plasma resonance of brass nanoparticles depends slightly on the type of laser source used for their synthesis and lies near 515 nm. The presence of brass nanoparticles in the liquid is corroborated by the x-ray diffractometry of the evaporated suspension.

Laser radiation acting on the ensemble of brass nanoparticles in the liquid changes their spectrum (Fig. 1). The peak corresponding to copper nanoparticles becomes noticeable. Upon further action on the colloidal solution, the peak corresponding to brass nanoparticles disappears, and only the plasma resonance peak of copper nanoparticles remains. Qualita-
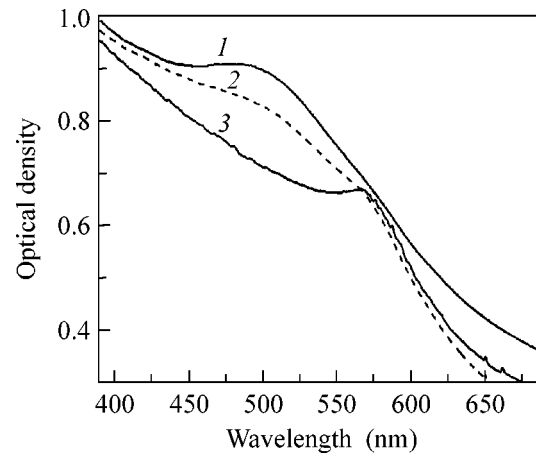

Fig. 1. Dynamics of the change in the spectrum of a colloidal solution of brass nanoparticles upon irradiation with the radiation of a Nd:YAG laser: (*1*) brass nanoparticles after production and (*2*) 10- and (*3*) 90-min action on the solution.

tive evidence of the effect is the absence of small brass nanoparticles (with a radius smaller than 5 nm) upon the laser ablation of a brass target in ethanol. Estimates show that the time of diffusion of zinc atoms to a distance of about the diameter of a nanoparticle in the liquid state is comparable with the duration of the radiation pulse of laser sources used in this work [12]. Small nanoparticles rapidly lose zinc upon laser irradiation and are transformed to copper nanoparticles oxidized by air oxygen. Generally speaking, the peak of copper nanoparticles is already distinguishable upon the production of brass nanoparticles by the ablation of the target in the liquid, which is corroborated by the decomposition of the absorption spectrum of the colloidal solution into components. They arise because brass nanoparticles repeatedly hit the laser beam, which leads to the separation of the components of the nanoparticle and removal of zinc from them in the process of the laser ablation of the brass target in the liquid.

Zinc removed from brass nanoparticles reacts with air oxygen dissolved in the surrounding liquid and with the liquid itself. As a result, the nanoparticles are covered by a shell consisting of the products of such a reaction. Figure 2 shows the typical form of shell nanoparticles produced upon the ablation of brass in ethanol. Shell nanoparticles can sometimes repeatedly hit the laser beam, which results in their fragmentation and the destruction of the shell. The shell fragments are also seen in Fig. 2. Leaving the nanoparticle, zinc is oxidized to ZnO, which corresponds to the absorption peak of the colloidal solution near 360 nm. The presence of ZnO in the liquid is also corroborated by the x-ray pattern of the evaporated suspension of nanoparticles.

The effect of the segregation of the components of alloy nanoparticles must obviously be manifested in the presence of small impurities whose melting tempera-
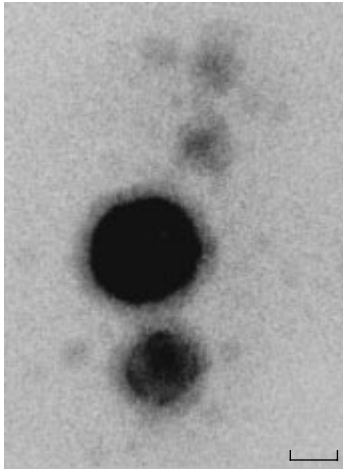
Fig. 2. Form of shell brass nanoparticles obtained by the ablation of a brass target in ethanol with the radiation of a copper-vapor laser. The image is obtained by a transmission electron microscope, and the scale mark corresponds to 10 nm.

ture is lower than the temperature of the basic substance of the nanoparticles. The joint action of the Laplace pressure and the pressure of liquid vapors surrounding the nanoparticle must result in the spatial redistribution of impurities within nanoparticles due to diffusion and their removal from the surface upon laser irradiation. The purity of the material of nanoparticles is expected to always be higher than the purity of the initial material due to the above effect. Note that the segregation effect itself is primarily caused by the smallness of nanoparticles, and laser heating only accelerates the diffusion process due to their melting.

REFERENCES

1. F. V. Bunkin, B. S. Luk'yanchuk, and G. A. Shafeev, Pis'ma Zh. Éksp. Teor. Fiz. **39**, 464 (1984) [JETP Lett. **39**, 563 (1984)].
2. S. D. Zakharov, M. A. Kazaryan, and N. P. Korotkov, Pis'ma Zh. Éksp. Teor. Fiz. **60**, 317 (1994) [JETP Lett. **60**, 322 (1994)].
3. A. V. Simakin, V. V. Voronov, G. A. Shafeev, *et al.*, Chem. Phys. Lett. **348**, 182 (2001).
4. F. Bozon-Verduraz, R. Briner, V. V. Voronov, *et al.*, Kvantovaya Élektron. (Moscow) **33**, 714 (2003).
5. K. V. Anikin, N. N. Melnik, A. V. Simakin, *et al.*, Chem. Phys. Lett. **366**, 357 (2002).
6. A. V. Simakin, V. V. Voronov, and G. A. Shafeev, in *Action of Laser Radiation on Absorbing Media*, Ed. by S. V. Garnov and A. A. Samokhin (Nauka, Moscow, 2004), Tr. Inst. Obshch. Fiz., Ross. Akad. Nauk, Vol. 60, p. 83 [in Russian].
7. A. V. Simakin, V. V. Voronov, N. A. Kirichenko, *et al.*, Appl. Phys. A **79**, 1127 (2004).
8. G. A. Shafeev, E. Freysz, and F. Bozon-Verduraz, Appl. Phys. A **78**, 307 (2003).
9. A. T. Izgaliev, A. V. Simakin, and G. A. Shafeev, Kvantovaya Élektron. (Moscow) **34**, 47 (2004).
10. T. Castro, R. Reifenberg, E. Choi, *et al.*, Phys. Rev. B **42**, 8548 (1990).
11. M. Wautelet, J. P. Dauchot, and M. Hecq, Nanotechnology **11**, 6 (2000).
12. *Physical Values: Handbook*, Ed. by I. S. Grigor'ev and E. Z. Meĭlikhov (Énergoatomizdat, Moscow, 1991) [in Russian].
13. S. S. Gorelik and M. Ya. Dashevskiĭ, *Materials Science of Semiconductors and Physical Metallurgy* (Metallurgiya, Moscow, 1973) [in Russian].
14. J. A. Creighton and D. G. Eadon, J. Chem. Soc. Faraday Trans. **87**, 3881 (1991).

Translated by R. Tyapaev

Dissipative Instability in an Aerosol Plasma

A. V. Gaponov-Grekhov and V. Yu. Trakhtengerts*

Institute of Applied Physics, Russian Academy of Sciences, ul. Ul'yanova 46, Nizhni Novgorod, 603950 Russia
* e-mail: vyt@appl.sci-nnov.ru
Received August 30, 2004; in final form, November 1, 2004

Dissipative instability in a weakly ionized aerosol plasma has been studied with allowance for a finite electric conductivity of the medium, electron and ion diffusion, and friction of the aerosol component against a neutral gas. Instability is caused by the relative drift of the aerosol and ion components. Estimates of the basic parameters of instability (threshold, characteristic wavelengths, and increments) in experiments with dust crystals indicate that this instability can be an important additional factor upon the formation of regular structures in an aerosol plasma. © *2004 MAIK "Nauka/Interperiodica"*.

PACS numbers: 52.27.Lw; 52.35.–g

Experiments devoted to the formation of regular structures, which are called dust crystals, in a partially ionized aerosol plasma have been actively discussed in recent years, and mechanisms of their formation have been analyzed (see reviews [1–5] and book [6]). In these experiments, aerosol particles have a large electric charge and make a significant contribution to charge balance, and their sizes are comparable with the mean free path of ions and atoms. Such a medium is also realized under natural conditions [2], in particular, in cumulonimbus and mesospheric clouds [7, 8].

We emphasize that the conditions of laboratory experiments, as well as observed effects, are very diverse. In some experiments, an electrostatic trap for dust particles, which is induced by an external field, plays the main role, and a dust crystal is formed due to interaction between particles through the screened Coulomb potential [6]. Attraction between identically charged particles in a wake can be substantial for the appearance of orientational order [9].

We consider a case with the relative drift of the aerosol and ion components, where collective effects can be manifested. This case is realized, e.g., in experiments where dust particles are injected into the space between two electrodes, and a partially ionized electron–ion plasma is formed under the action of a microwave field [10–14]. The initial state includes a charged aerosol component, which is almost in a suspension state where gravity is compensated by friction and force induced by the electric field, and drift flows of electrons and ions, which arise in this field. The negative charge of a dust particle is sustained by balance between electron and ion flows onto its surface, and the constant electric field is associated with the deposition of charged dust particles and plasma onto the isolated lower electrode. The sizes of the regular structures observed in these experiments are much larger than the mean free path of ions; i.e., we have a dissipative medium where dissipation is attributed to finite electric conductivity, as well as to electron and ion diffusion.

Electronic experience [15, 16] shows that, in the presence of an electron flow, dissipative instability is realized in such a medium. This instability has a number of features as compared to instabilities in a collisionless plasma. These are a broad band, the absence of exact synchronism between a wave and a flow, and a weak dependence on the parameters of the medium. This means that dissipative instability is much more universal than resonance (collisionless) instabilities. The dissipative instability of an electron beam in a medium with finite electric conductivity was apparently analyzed in electronics (see review [15]). When collisions in the electron beam are absent and diffusion in the background medium is negligible, this instability has threshold. In [16], a mechanism of mutual attraction between moving electrons and oscillators in a conducting medium was discussed. This mechanism can also be substantial in an aerosol plasma.

The aim of this work is to analyze the conditions under which dissipative instability is realized when the drift of charged aerosol particles with respect to the ion component of the medium plays the role of the electron beam and dissipation is attributed to finite electric conductivity, the friction of the aerosol flow against the neutral gas, and the diffusion of the electron and ion components. Friction results in the appearance of an instability threshold in the concentration and charge number of aerosol particles [7]. Diffusion increases the threshold and significantly affects the dispersion properties of excited electrostatic waves [8]. In our opinion, these processes are determining in the above experiments with dust crystals [10–14].

As is well known [2–6], the hydrodynamics of an aerosol (complex) plasma can substantially differ from the classical hydrodynamics of a multicomponent plasma, because the system is open and additional

forces appear due to the deposition of electrons and ions onto the surface of aerosol particles and the charge of particles becomes a dynamic variable. However, previous experience [17] and preliminary estimates for the conditions of experiments [10–14] show that these additional factors do not change the fundamental features of dissipative instability and can only change certain numerical estimates. For this reason, we consider the problem in the framework of the classical hydrodynamics of a multicomponent plasma, neglecting any change in the charge of aerosol particles and absorption of the plasma on its surface. For the Fourier harmonic of an electrostatic disturbance characterized by the electric field $\mathbf{E}$ that is parallel to the wave vector $\mathbf{k}$ and proportional to $\exp\{-i\omega t + i\mathbf{k}\mathbf{r}\}$ in the linear approximation in $\mathbf{E}$, it is easy to derive the dispersion relation between $\mathbf{k}$ and frequency ω. In view of the above initial state of the medium, this equation in the coordinate system where dust particles are initially at rest is written as (see also [8])

$$
1 - \frac{\Omega_p^2}{\omega(\omega + i\nu_a)} + \frac{4\pi\sigma_i i}{(\omega - \mathbf{k}\mathbf{V}_i) + ik^2 D_i}
+ \frac{4\pi\sigma_e i}{(\omega - \mathbf{k}\mathbf{V}_e) + ik^2 D_e} = 0,
\tag{1}
$$

where $\Omega_p = (4\pi Z_a^2 e^2 N_a / M_a)^{1/2}$ is the plasma frequency of aerosol particles; M_a, N_a, and Z_a are the mass, concentration, and charge number of these particles, respectively; ν_a is the effective collision frequency characterizing the friction associated with the motion of an aerosol particle in the surrounding gas; and $\sigma_{e(i)}$, $D_{e(i)}$, and $V_{e(i)}$ are the electric conductivity, diffusion coefficient, and velocity of electrons (ions). Equation (1) was derived disregarding the thermal motion and scatter of aerosol particles according to size. The role of these effects will be discussed below.

We emphasize that, in the experiments with dust particles under discussion, electrons between electrodes, except a small fraction $\Delta n_e \sim (m/MT_i/T_e)^{1/2} n_i \sim 10^{-3} n_i$ (where m and M are the masses of an electron and an ion, respectively; T_e and T_i are the temperatures of the electron and ion, respectively; and n_i is the ion concentration) that ensures the compensation of the ion current to the lower electrode, exhibit a Boltzmann distribution with the characteristic scale that is equal to the distance between electrodes and drift velocity $V_e \approx 0$. In addition, estimates show that the inequality

$$
\omega \ll k^2 D_e,
\tag{2}
$$

is valid in nearly all experiments. In this approximation, a quite complete analytical analysis of Eq. (1) is possible. At the instability threshold, when $\mathrm{Im}\,\omega = 0$, Eq. (1) in approximation (2) gives

$$
1 - \frac{\Omega_p^2}{(\omega^2 + \nu_a^2)} + \frac{4\pi\sigma_i D_i k^2}{(\omega - \mathbf{k}\mathbf{V}_i)^2 + k^4 D_i^2} + \frac{4\pi\sigma_e}{k^2 D_e} = 0,
\tag{3}
$$

$$
\frac{\Omega_p^2 \nu_a}{\omega(\omega^2 + \nu_a^2)} + \frac{4\pi\sigma_i(\omega - \mathbf{k}\mathbf{V}_i)}{(\omega - \mathbf{k}\mathbf{V}_i)^2 + k^2 D_i} = 0.
\tag{4}
$$

From the system of equations (3) and (4), one can derive the following dispersion relation $\omega(\mathbf{k})$ for an electrostatic wave at the instability threshold:

$$
\omega = \mathbf{k}\mathbf{V}_i\left(1 - \frac{1}{2\Delta} \pm \sqrt{\frac{1}{4\Delta^2} - \frac{D_i \nu_a}{V_L^2 \Delta}}\right),
\tag{5}
$$

where

$$
\Delta = 1 + \frac{\nu_a}{4\pi\sigma_i}\left(1 + \frac{1}{k^2 \lambda_{De}^2}\right),
\tag{6}
$$

$V_L = (\mathbf{k}\mathbf{V}_i)/|\mathbf{k}|$, $\lambda_{De} = V_{Te}/\omega_{pe}$ is the electron Debye radius, where V_{Te} and ω_{pe} are the thermal velocity and plasma frequency for electrons, respectively. Under the conditions we discussed, the parameter Δ is close to unity and the second term of the radicand in Eq. (5) is much less than unity. Correspondingly, solution (5) contains two modes, fast (sign +) and slow (sign –). The slow mode ($\omega \ll \mathbf{k}\mathbf{V}_i$) has the lowest threshold and will be analyzed more carefully. In the limit

$$
\frac{4 D_i \nu_a}{V_L}\Delta \ll 1, \quad \Delta - 1 \ll 1
\tag{7}
$$

the dispersion relation for this mode is written as

$$
\omega = \frac{\nu_a(\mathbf{k}\mathbf{V}_i)}{4\pi\sigma_i}\left[1 + \frac{1}{k^2 \lambda_{De}^2} + B^{-1}\right],
\tag{8}
$$

where $B = \nu_{in}^2 V_L^2 / \omega_{pi}^2 V_{Ti}^2$. Substituting Eq. (8) into Eqs. (3) and (4), we obtain the instability threshold

$$
\left(\frac{\Omega_p^2}{\nu_a^2}\right)_{\mathrm{thr}} = \left(1 + \frac{1}{k^2 \lambda_{De}^2} + \frac{1}{B + k^2 \lambda_{Di}^2}\right)\left(1 + \frac{\omega^2}{\nu_a^2}\right),
\tag{9}
$$

where $\lambda_{Di} = V_{Ti}/\omega_{pi}$ is the ion Debye radius and ω is given by Eq. (8).

From Eq. (9), the optimum wavenumber k_{opt} corresponding to the lowest threshold can be determined. In experiments with dust crystals, the conditions

$$
k^2 \lambda_{Di}^2 \ll 1, \quad B \gtrsim 1, \quad P \equiv \frac{\lambda_{Di}^2}{\lambda_{De}^2} B \ll 1
\tag{10}
$$

Table

p, mbar	r_a, cm	E_0, V/cm	n_i, cm^{-3}	ν_{in}, s^{-1}	V_{Ti}, cm/s	n_e, cm^{-3}	N_a, cm^{-3}	V_{Di}, cm/s	ν_a, s^{-1}	Z	B
1	7×10^{-4}	7	10^9	10^7	3×10^4	6×10^8	4×10^4	3×10^4	30	~10^4	~1

are usually valid. In view of these inequalities, we obtain

$$\left(\frac{\Omega_p^2}{\nu_a^2}\right)_{\mathrm{thr}}^{\min} \approx \left(1 + \frac{1}{B}\right)\left[1 + P^{\frac{1}{2}}\left(1 + \frac{1}{B}\right)^{\frac{1}{2}}\right] \qquad (11)$$

and

$$k_{\mathrm{opt}}^{-1} = \left[B + 3 + \frac{3}{B}\right]^{-\frac{1}{4}}(\lambda_{Di}\lambda_{De})^{1/2}. \qquad (12)$$

Near threshold, the instability increment γ_m is determined by the expression

$$\gamma_m \approx \frac{\omega_{\mathrm{opt}}^2}{\nu_a}\left\{\frac{\Omega_p^2}{\nu_a^2} - \left(\frac{\Omega_p^2}{\nu_a^2}\right)_{\mathrm{thr}}^{\min}\right\}, \qquad (13)$$

where ω_{opt} is given by Eq. (8) for $k = k_{\mathrm{opt}}$ determined from Eq. (12).

On the basis of the above analysis, we discuss the possibility of realizing the instability under consideration in experiments with dust crystals. Dust crystals were first observed by Thomas *et al.* [10, 11] and Chu and Lin [12]. In [10, 11], the setup included two planar electrodes between which a microwave source induced a weakly ionized plasma with an ion concentration of $n_i \sim 10^9$ cm^{-3} at a pressure of about 2 mbar. Dust particles were injected from the upper electrode. Their size and concentration were equal to 7 ± 0.2 μm and about ~4×10^4 cm^{-3}, respectively. The charge number of particles was not measured but was estimated as $Z \sim 10^4$– 3×10^4. The plasma was strongly nonisothermal: the electron temperature was equal to $T_e \sim 3$ eV and the temperature of ions and dust particles was equal to $T_e \sim$ 0.03 eV. A potential of $U \sim -14$ V was induced on the isolated lower electrode. This potential corresponds to an average electric field of $E_0 \sim 7$ V/cm for a 2-cm gap between electrodes. A dust crystal with a regular (periodic) distribution of dust particles over a horizontal plane with a lattice constant of $\delta \approx 250$ μm was observed in the lower part of the gap and included up to 16 layers along the vertical.

The above information is enough to compare experimental data with the instability under consideration, in particular, to determine the threshold, optimum scale, and increment of instability. A missing element of Eqs. (8) and (11)–(13) is the expression for the effective collision frequency ν_a. In a sufficiently dense medium, where the mean free path of a molecule $l = V_T/\nu_n$ is much shorter than the dust-particle radius r_a, the Stokes force and, correspondingly, an effective collision frequency of $\nu_a \approx 6\pi\eta r_a/M_a$, where η is the dynamic viscosity, are good approximations. In experiments with dust crystals, the inequality $l \geq r_a$ is sometimes satisfied. For this reason, we generalize ν_a by the expression

$$\nu_a \approx \frac{6\pi\eta r_a^2}{(r_a + 2l)M_a}, \qquad (14)$$

which, in the limit $2l > r_a$ and in view of the expression $\eta = \frac{1}{3}mnV_T l$, takes the form of the classical formula for spherical particles, $\nu_a \approx (m/M)\pi r_a^2 nV_T$, where m, n, and V_T refer to neutral molecules of the gas medium. For a known electric field E_0, it is easy to estimate the drift velocity of ions, which is determined by ion mobility. This velocity is much higher than the fall velocity of dust particles. The table presents the parameters used to estimate the threshold, characteristic scale, and increment of instability.

Using the indicated values, we obtain $\Omega_p^2/\nu_a^2 \approx 3$ for the conditions of the experiment reported in [11]. According to Eq. (11), the threshold value is equal to $(\Omega_p^2/\nu_a^2)_{\mathrm{thr}} \approx 2.2$. Assuming that the lattice constant δ is determined by the interference of counterpropagating (in the horizontal direction) waves, it can be determined as

$$\delta = \frac{\pi}{k_{\mathrm{opt}}}. \qquad (15)$$

Using Eq. (12), we obtain $\delta \sim 600$ μm. It is much larger than the observed value $\delta \sim 250$ μm. However, closer quantitative agreement can be achieved by multiplying n_i used in estimates by a factor of 4 in view of the possible spread of the parameters (e.g., n_i was given in [11] with an accuracy to a factor of 4). Using Eq. (13), the characteristic time of developing instability can be estimated for the experiment under consideration. For the parameters $\Omega_p^2/\nu_a^2 - (\Omega_p^2/\nu_a^2)_{\mathrm{thr}}^{\min} \approx 0.2$ and $\omega_m \approx 5$ s^{-1}, we obtain $\gamma_m \approx 0.17$ s^{-1}.

The development of instability results in the concentration of identically charged particles, including dust particles, into clusters. However, this clustering does not guarantee the formation of 3D structures observed in experiments. In this case, in addition to linear theory, nonlinear calculations are likely necessary. However, certain conclusions on the structural features of the

instability-induced electric potential can be made using linear theory. From the dispersion relation given by Eq. (8), we calculate the group velocity of excited waves. Taking into account that $k^2 \lambda_{De}^2 \gg 1$, in the coordinate system with the z axis along the ion drift direction, we obtain

$$V_{gz} \equiv \frac{\partial \omega}{\partial k_z} = q\left(1 + b - b\frac{k_\perp^2}{k_z^2}\right), \quad V_{g\perp} \equiv \frac{\partial \omega}{\partial k_\perp} = 2qb\frac{k_\perp}{k_z}, \quad (16)$$

where

$$q = \frac{\nu_a E_0}{4\pi e n_i}, \quad b = \frac{4\pi e n_i T_i}{E_0^2}. \quad (17)$$

In Eqs. (17), we take into account that the ion drift velocity in the electric field is given by $V_i = eE_0/m_i\nu_{in}$.

For the experiment reported in [11], V_{gz} at $k_\perp = 0$ is estimated as $V_{gz}(k_\perp = 0) \approx 2.6$ cm/s. For a characteristic vertical scale of 1 cm, instability can develop only if $V_{gz} \longrightarrow 0$, i.e., for oblique waves for which

$$k_\perp = \pm k_z\sqrt{1 + b^{-1}}, \quad b \sim 1. \quad (18)$$

Thus, the formation of 3D "crystalline" structures similar to those observed in the experiment reported in [11] can be expected even in the linear approximation with allowance for axial symmetry. A more rigorous analysis requires the inclusion of finite sizes and boundary conditions in the transverse plane of the system.

Let us briefly discuss the results of the other experiments that were reported in [12–14] and conducted under conditions close to those described in [10, 11]. The lattice constant of dust crystals is the most suitable parameter for comparison. In [12], the ion concentration was double or triple that in [11], and the lattice constant was half the corresponding value. In [13], the ion concentration was noticeably lower than that in [11] and was equal to 2×10^8 cm^{-3}. In this case, the lattice constant was equal to $\delta \approx 800$ μm. Such a dependence on n_i qualitatively agrees with formula (12) for the optimum scale of unstable waves.

An interesting effect of the "melting" of a dust crystal was observed in the experiment reported in [14]. The authors reduced the gas pressure, which resulted in the intense heating of dust particles due to a decrease in thermal losses upon interaction with the neutral gas. In this case, dislocations in the structure arose first, and then, with a further decrease in pressure, the crystal was destroyed; i.e., the disordered motion of dust particles began. In terms of the above mechanism, this destruction could be attributed to the breakdown of instability upon an increase in the thermal scatter of dust particles. In the hydrodynamic approximation, such a breakdown occurs when

$$kV_{Ta} > \omega, \quad (19)$$

where $V_{Ta} = (T_a/M_a)^{1/2}$ is the thermal velocity of dust particles. Near the instability threshold, optimum values k_{opt} (12) and $\omega_{opt} \approx \nu_a k_{opt} V_i(1 + B^{-1})/4\pi\sigma_i$ (8) are taken for k and ω, respectively. The destruction of the crystal was observed at $T_a \sim 3$ eV in [14]. Substituting the values $\omega_{opt} \approx 5$ s^{-1} and $k_{opt} \approx 50$ cm^{-1} into Eq. (19), we obtain $\omega/k \sim V_{Ta} \sim 0.1$ (cm/s); i.e., the breakdown of instability is really possible.

Summarizing the above analysis, we conclude that the instability under consideration could be manifested in the experiments with the dust plasma reported in [10–14]. Moreover, the parameters of unstable waves are in good quantitative agreement with the structural features of dust crystals. At the same time, the usual presence of only one particle in each site of the dust crystal is inconsistent with the character of the clustering of particles under the conditions of developed instability. Moreover, the destruction observed for the crystal upon the enhancement of thermal motion occurs at two stages: translational order is destroyed first and, then, orientational order is destroyed. This behavior is not completely explained in terms of wave disturbances and shows that the conditions of formation of ordered structures were reached in the subthreshold region (with respect to dissipative instability) in the experiments reported in [10–14]. Under the condition of instability development, it should be expected that several (many) initial particles will combine into clusters and adhere together, forming larger particles. Such a possibility was corroborated in certain experiments where the clustering of aerosol particles, which had large negative charge, was observed [2]. For a more definite answer to the above questions, it is likely necessary to more carefully investigate the initial stage of formation of a dust crystal in experiments and the dependence of the formation process on the dust-particle concentration as well as to measure the dynamic structure of the spatial ion charge.

REFERENCES

1. A. P. Nefedov, O. F. Petrov, and V. E. Fortov, Usp. Fiz. Nauk **167**, 1215 (1997) [Phys. Usp. **40**, 1163 (1997)].

2. V. N. Tsytovich, Usp. Fiz. Nauk **167**, 57 (1997) [Phys. Usp. **40**, 53 (1997)].

3. V. N. Tsytovich, G. E. Morfill, and H. Thomas, Fiz. Plazmy **28**, 675 (2002) [Plasma Phys. Rep. **28**, 623 (2002)].

4. G. E. Morfill, V. N. Tsytovich, and H. Thomas, Fiz. Plazmy **29**, 3 (2003) [Plasma Phys. Rep. **29**, 1 (2003)].

5. H. Thomas, G. E. Morfill, and V. N. Tsytovich, Fiz. Plazmy **29**, 963 (2003) [Plasma Phys. Rep. **29**, 895 (2003)].

6. V. E. Fortov, A. G. Khrapak, and I. T. Yakubov, *Physics of Nonideal Plasma* (Fizmatlit, Moscow, 2004) [in Russian].

7. V. Yu. Trakhtengerts, Dokl. Akad. Nauk SSSR **308**, 584 (1989).

8. V. Yu. Trakhtengerts, J. Atmos. Terr. Phys. **56**, 373 (1994).

9. S. V. Vladimirov and M. Nambu, Phys. Rev. E **52**, 2172 (1995).

10. G. E. Morfill, in *Proceedings of XX International Conference on Phenomena in Ionized Gases* (Pisa, Italy, 1991).

11. H. Thomas, G. E. Morfill, and V. Demmel, Phys. Rev. Lett. **73**, 652 (1994).

12. J. H. Chu and I. Lin, Physica A (Amsterdam) **205**, 183 (1994).

13. A. Melzer, T. Trottenberg, and A. Piel, Phys. Lett. A **191**, 301 (1994).

14. H. M. Thomas and G. E. Morfill, Nature **379**, 806 (1996).

15. V. M. Lopukhin and A. A. Vedenov, Usp. Fiz. Nauk **53**, 69 (1954).

16. A. V. Gaponov-Grekhov, I. S. Dolina, B. E. Nemisov, and L. A. Ostrovskii, Zh. Éksp. Teor. Fiz. **102**, 243 (1992) [Sov. Phys. JETP **75**, 128 (1992)].

17. E. A. Mareev, A. E. Sorokin, and V. Yu. Trakhtengerts, Fiz. Plazmy **25**, 289 (1999) [Plasma Phys. Rep. **25**, 261 (1999)].

Translated by R. Tyapaev

Strong Spin Triplet Contribution of the First Removal State in the Insulating Regime of Bi₂Sr₂Ca₁₋ₓYₓCu₂O₈₊δ[¶]

C. Janowitz[1], U. Seidel[1], R.-S. T. Unger[1], A. Krapf[1], R. Manzke[1], V. Gavrichkov[2], and S. Ovchinnikov[2]

[1] *Institute of Physics, Humboldt University of Berlin, 12489 Berlin, Germany*
[2] *Kirensky Institute of Physics, Russian Academy of Sciences, Krasnoyarsk, 660036 Russia*
e-mail: gav@iph.krasn.ru
Received October 6, 2004

The experimental dispersion of the first removal state in the insulating $Bi_2Sr_2Ca_{1-x}Y_xCu_2O_{8+\delta}$ regime is found to differ significantly from that of other parent materials: oxyclorides and La_2CuO_4. For Y contents of $0.92 \geq x \geq 0.55$ due to nonstoichiometric effects in the Bi–O layers, the hole concentration in the CuO_2 layers is almost constant and, on the contrary, the crystal lattice parameters a, b, c change very strongly. This (a, b) parameter increase and c parameter decrease results in an unconventional three peak structure at $(0, 0)$, $(\pi/2, \pi/2)$, (π, π) for $x = 0.92$. We can describe the experimental data only beyond the framework of the three-band p–d-model involving the representations of a new triplet counterpart for the Zhang–Rice singlet state. © *2004 MAIK "Nauka/Interperiodica".*

PACS numbers: 73.20.At; 74.25.Jb; 74.62.Dh; 79.60.Bm

Until now in high-T_c cuprates, there has not been any clear evidence that there is a contribution to the first removal state from states distinct from the Zhang–Rice singlet (ZRS) A_{1g} state. Early theoretical works [1–4] indicating the possible approach of the ZRS and the $^3B_{1g}$ two-hole states remained without any experimental support. Interestingly, the simple inversion of the triplet and singlet states should be accompanied by a change in the type of magnetic ordering already in undoped parent structures. The question on the type of magnetic ordering or magnetic and quasiparticle excitations spectra in the case of their approach has never been investigated since this problem cannot be studied within the framework of the three-band p–d- and t–J-models.

Accordingly, theoretical descriptions have been developed for antiferromagnetic (AF) insulators La_2CuO_4 and $Sr_2CuO_2Cl_2$ leading to states with the periodicity of the AF Brillouin zone [5, 6], i.e., maxima at $\mathbf{k} = (\pi/2, \pi/2)$. Our systematic high resolution ARPES (angle resolved photoemission) study of $Bi_2Sr_2Ca_{1-x}Y_xCu_2O_{8+\delta}$ ($x > 0.55$) shows additional new states at $\mathbf{k} = (0, 0)$ and $\mathbf{k} = (\pi, \pi)$. In contrast to La_2CuO_4, in $Bi_2Sr_2Ca_{1-x}Y_xCu_2O_{8+\delta}$, the hole concentration per Cu x_h is smaller than a substitution concentration x because some holes induced by $Ca^{+2} \longrightarrow Y^{+3}$ substitution go to the Bi–O layers. For example, in the insulator region $1 \geq x \geq 0.5$, the value n_h changes very weakly by $0.02 \leq n_h \leq 0.05$ [7]. Nevertheless, changes in the crystal lattice parameters are induced by the com-

position variable x, leading to an (a, b)-parameter increase and c-parameter decrease with increasing Y concentration x [8]. As a consequence, the hopping parameters t_{pp} (in-plane O–O hopping) and t'_{pp} (in-plane O–out-of-plane O hopping) also vary with the lattice parameters. Thus, in $Bi_2Sr_2Ca_{1-x}Y_xCu_2O_{8+\delta}$, at almost constant hole concentration, the reduction of the relation d_{pl}/d_{ap} (Cu–in-plane O and Cu–out-of-plane O distances) or so-called "chemical" pressure effect takes place. It is, according to [1–4], one of the main reasons for the approach of the singlet and triplet states. $Bi_2Sr_2Ca_{1-x}Y_xCu_2O_{8+\delta}$ single crystals were grown from the melt (for details see [9]). By replacement of the bivalent calcium with trivalent yttrium, the hole concentration of the CuO_2 planes has been controlled in the samples. The superconducting properties respectively the disappearance of superconductivity with doping were proven by susceptibility measurements. The stoichiometry and, in particular, the Y content were determined by energy dispersive X-ray analysis (EDX). For an Y content of $0.92 \geq x \geq 0.55$, the crystals showed no superconducting transition in susceptibility. The samples were rectangularly shaped with the long side along the crystallographic a axis, confirmed by diffraction experiments, and had a typical size of 5×2. Crystals were cleaved in UVH ($p = 1 \times 10^{-10}$ mbar) and were measured at a temperature of 90 K. No effects due to charging of the samples have been observed. LEED and Laue patterns revealed sharp spots for all doping concentrations. An example is given in Figs. 1d and 1e. Since all samples showed about a 1×5 reconstruction,

---

[¶] This article was submitted by the authors in English.
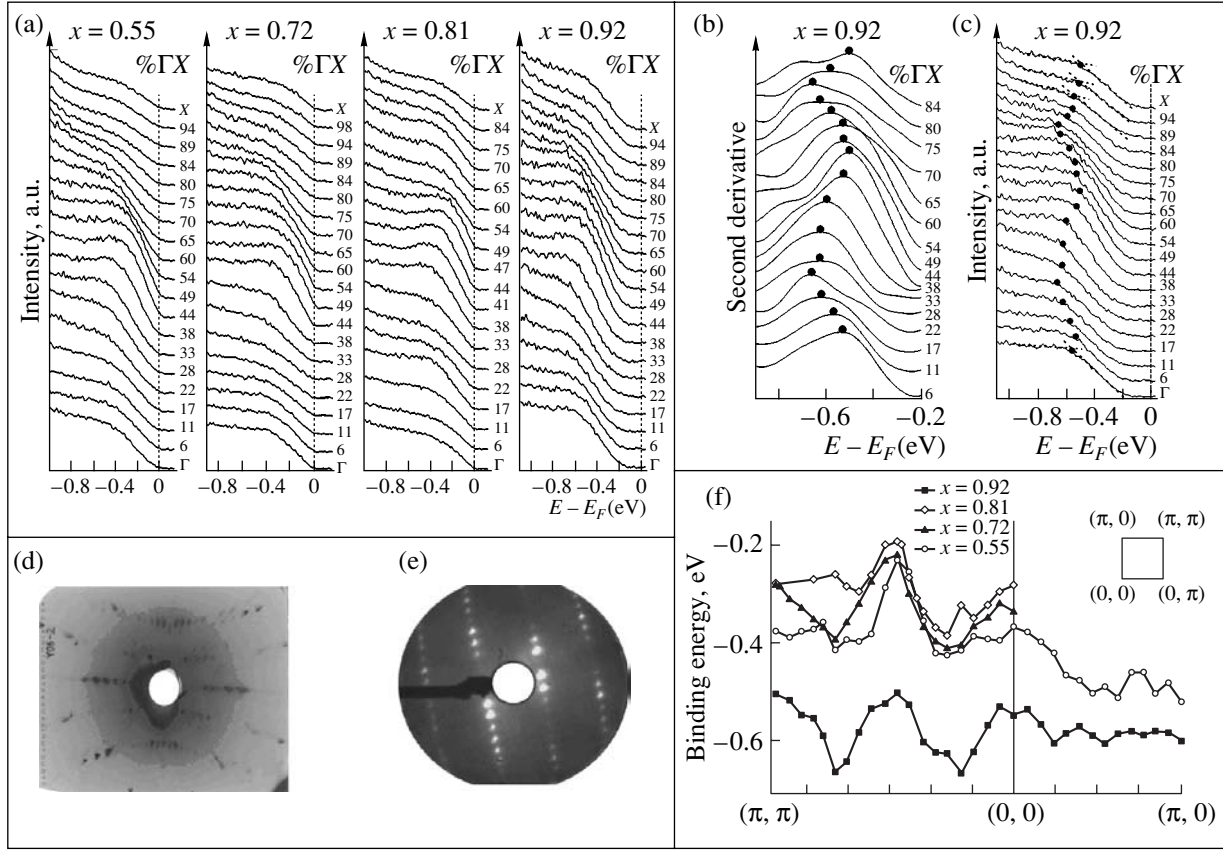
Fig. 1. (a) EDCs of $Bi_2Sr_2Ca_{1-x}Y_xCu_2O_{8+\delta}$ single crystals in the insulating phase taken along the ΓX $(0, 0) \longrightarrow (\pi, \pi)$ direction of the Brillouin zone for different Y content at $T = 90$ K. With increasing Y concentration, the number of holes in the CuO_2 plane decreases. The polarization plane of the synchrotron radiation was in the ΓM $(0, 0) \longrightarrow (\pi, 0)$ direction. (b) Second derivative of a selection of spectra from (c) multiplied by a factor of minus one. The maxima are marked by a dot. (c) Spectra along the ΓX direction of the sample with the highest Y concentration ($x = 0.92$). The positions of the centroids have been obtained either from the maxima of (b) (derivative method) or as the intersection of the tangents (tangent method). In the latter case, this has been indicated by two straight lines in (c). (d) Example of a typical LEED picture for a single crystal with Y concentration $x = 0.72$ at an electron energy of 70 eV. (e) Example of a typical Laue pattern for a single crystal with Y concentration $x = 0.72$. (f) Dispersion of the uppermost CuO derived states as obtained from the spectra of (a) along the major symmetry lines. The ΓM dispersions are from spectra not shown.

the spectra were recorded along the ΓX and not along the ΓY direction to avoid contributions of superstructure bands. The ARPES experiments have been performed at the $3m$ normal-incidence monochromator HONORMI at beamline *W3.2* of HASYLAB. For the measurements discussed here, a photon energy of 18 eV was used. The energy distribution curves (EDC) were recorded with a hemispherical deflection analyzer with a total acceptance angle of 1° and an energy resolution of 10 meV [10]. Due to the broader emission maxima of insulating HTSCs, an overall resolution (analyzer plus monochromator plus temperature) of 80 meV was sufficient in order to improve statistics. An *AU* Fermi edge served as the Fermi energy reference.

Because the photoemission line shape of high temperature superconductors at arbitrary doping levels is not well understood, there is a strong need for a reliable data analysis procedure that gives a reasonable approximation of the real physics but does not lead to wrong

conclusions. It is at present not known whether a spectrum for a given doping level can be interpreted in terms of single-particle excitations. The objective is, therefore, simply to define approximate quantities that reflect the energy scale of the data. The centroid (the center of gravity) of spectral features and positions of leading edges are the obvious possibilities. In the recent literature, a rather simple model consisting of a Lorentzian sitting on a step-edge background has been adopted to model the broad dispersing structures observed for insulating and underdoped cuprates [11]. It has been found [12] that, even in highly under-doped samples, the change in the slope of the spectra is a characteristic that easily identifies the broad high-energy feature. This procedure is illustrated in Fig. 1c by the dashed intersecting tangents, which approximate the up and down slope of the spectra (tangent method). It is thereby assumed that the steeper the slope, the closer the ZRS band to the Fermi energy. An alternative

method is to take the minima of the second derivative of the smoothed spectra (derivative method). This method to determine dispersion was, for instance, recently applied by Ronning *et al.* [5]. An example of this method is given in Fig. 1b, which shows a selection of second derivatives from the spectra of Fig. 1c (the derivatives were multiplied by minus one to obtain peaks). We used this method preferentially. Only in cases where the second derivatives came out too broad or as double structures, as was the case for the Γ spectrum and the three spectra at the highest angles from Fig. 1c, was the tangent method used. A comparison of both methods on the same spectra yielded approximately the same results. The intersection of the two slopes (tangent method) showed a systematic 30–60 meV shift to higher binding energies when compared to the derivative method. The typical error from the tangent method was 100 meV and from the derivative method between 60 meV and 100 meV. A detailed report will be given in a forthcoming publication.

In Fig. 1, series of spectra of the insulating state of the $Bi_2Sr_2Ca_{1-x}Y_xCu_2O_{8+\delta}$ single crystals are shown for the ΓX direction ($(0, 0) \longrightarrow (\pi, \pi)$) of the Brillouin zone (panel (a)). The origin of the dispersing spectral weight near the Fermi level is due to strongly correlated CuO states located in the CuO_2 planes. While for low Y content and optimum doped crystals with the highest T_c ($x \leq 0.2$) the well-established Fermi level crossing is observed at about 0.4 ΓX (not shown), the insulators with $x \geq 0.55$ investigated here reveal no spectral weight at the Fermi energy. But the dispersing ZRS band is still present. The centroid of the ZRS bands of all insulators with Y content of $0.92 \geq x \geq 0.55$ is shifted to about the same binding energy of 300 meV. At a point halfway between Γ and (π, π), these insulators exhibit a distinct maximum in their dispersions, which is most pronounced for $x = 0.55$. With increasing c (decreasing hole concentration), the dispersion curves begin to rise around the $(0, 0)$ and (π, π) points of the Brillouin zone.

A dramatic change is observed for the $x = 0.92$ insulator. The centroid of the band has now been shifted to about 600 meV, and instead of one dominating maximum in the dispersion curve, three equally strong maxima are observable at positions $(0, 0)$, $(\pi/2, \pi/2)$, and (π, π) of the Brillouin zone. While the 600 meV shift is hard to ascribe to a definite reason and is possibly due to pinning by defects [5], the appearance of this new state is exciting and new. Around $x = 0.92$, the insulator is supposed to cross the boundary from the non-AF insulating to the AF insulating phase. In the AF state,

the next-nearest-neighbor copper atoms have antiparallel spin orientation coupled by a superexchange interaction via oxygen. The Wigner–Seitz cell then becomes twice as large and, as a consequence, the first Brillouin zone (BZ) is reduced by a factor of two and rotated by 45° [13]. If the underlying AF Brillouin zone were the only reason for the change in dispersion, the maximum at $(\pi/2, \pi/2)$ as in the oxychlorides could be explained, but not the developing maxima at $(0, 0)$ and (π, π). The above findings are therefore not similar to the observations in the oxychloride $Sr_2CuO_2Cl_2$ [5, 6, 14], which has been thought to behave like the parent compound of high-T_c cuprates. Despite the fact that the absolute maximum of the dispersion curve is also in $Sr_2CuO_2Cl_2$ at 0.5 ΓX, the band energy as well as the bandwidth are at variance with the insulating $Bi_2Sr_2Ca_{1-x}Y_xCu_2O_{8+\delta}$ samples.

All our attempts to obtain the three peaks in the dispersion at $(0, 0)$, $(\pi/2, \pi/2)$, and (π, π) in the framework of the t–t'–t''–J model failed. That is why we started with a more general model, the five-band p–d-model that takes into account Cu $d_{x^2-y^2}$, d_{z^2}, in-plane O p_x, p_y, and apical O p_z single-hole atomic states. The effect of strong electron correlations is certainly very important in the insulating phase, and in the framework of the multiband p–d-model, the generalized tight binding (GTB) method takes into account different intra-atomic Coulomb and Hund exchange interactions at Cu and O sites as well as Cu–O nearest neighbor repulsion. While in the three-band p–d-model the top of the valence band is formed by a dispersion of holes excited into the ZRS state, the new physics in the multiband p–d-model results from the $^3B_{1g}$ triplet contribution. The triplet counterpart for the ZRS is also known in the three-band p–d-model with energy much higher than the ZRS, $\Delta E = E_T - E_S \approx 2$ eV, so the triplet is not relevant in the low-energy region. This irrelevance appears to be a model-dependent result. In the multiband model presented here, ΔE sharply decreases due to Hund exchange contributions from the $d^\uparrow_{x^2-y^2} d^\uparrow_{z^2}$ configuration and additional bonding with apical oxygen-induced t'_{pd} and t'_{pp} hopping (here prime refers to the p_z apical orbital). For realistic parameters fitted well to the ARPES results for $Sr_2CuO_2Cl_2$ [15], the value $\Delta E \approx 0.7$ eV, and excitation of the extra hole added to b_{1g}, the initial state to the $^3B_{1g}$ triplet state gives a strong admixture near the $(0, 0)$ and (π, π) points to the ZR singlet. To describe the ARPES in the insulating phase of $Bi_2Sr_2Ca_{1-x}Y_xCu_2O_{8+\delta}$, we take into account the strong lattice parameter dependence on the Y content (parameter c decreases and in-plane parameters a, b increase with the Y concentration x [8]) and neglect the small changes in the hole concentration. The corresponding changes of the in-plane oxygen t_{pp} hopping and the in-plane apical oxygen hopping t'_{pp} are given in the table.
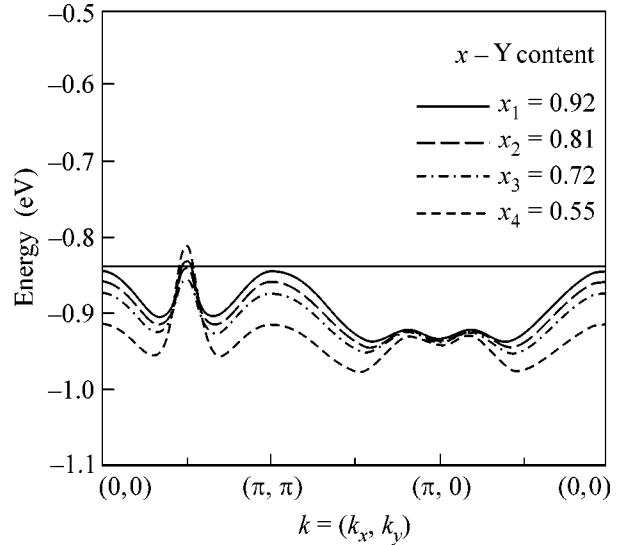
Table

Y content	0	0.55	0.72	0.81	0.92
t_{pp}	0.45	0.35	0.34	0.33	0.32
t'_{pp}	0.42	0.44	0.45	0.47	0.48

For simplicity, the other model parameters are the same as in the undoped CuO_2 layer [15]. The dispersion of the top of the valence band for different Y concentration is then calculated by the *GTB* method and is shown in Fig. 2. With increasing Y content, the three-peak structure along the direction $(0, 0) \longrightarrow (\pi, \pi)$ is clearly observed with the $(\pi/2, \pi/2)$ peak slightly decreasing its energy. Along the $(\pi, \pi) \longrightarrow (\pi, 0)$ line, there is no significant effect of the Y substitution. These results are in a good agreement with the ARPES data. Both states mix well to the one band of first removal states, in spite of the fact that there is a significant difference between them.

To clarify the triplet vs. singlet contribution, we have calculated the partial spectral weight contributions to the ARPES peaks (Fig. 3). The spectral function for the $(\pi/2, \pi/2)$ peak is determined mostly by the singlet, as in the *t–J* model. The main contribution to the $(0, 0)$ and (π, π) peaks is given by the triplet $^3B_{1g}$ and this contribution grows with increasing x. Figure 4 gives a comparison between experiment and theory for the dispersion of the crystals with the highest ($x = 0.92$) and lowest ($x = 0.55$) Y concentration along $(0, 0) \longrightarrow (\pi, \pi)$. The spectrum for the $x = 0.92$ sample has been shifted to equal minimum binding energy with the $x = 0.55$ spectrum in the manner also applied by Ronning *et al.* [5]. It can be seen very clearly from Figs. 3 and 4 that the dispersion at $(0, 0)$ and (π, π) changes considerably, because the new contribution of triplet states becomes detectable due to its increased spectral weight. To conclude, we have measured that, due to the "chemical" pressure effect induced by Y substitution in $Bi_2Sr_2Ca_{1-x}Y_xCu_2O_{8+\delta}$, the dispersion of the first removal state shows, at least near the AF phase at $x = 0.92$, a pronounced three-peak structure at the $(0, 0)$, $(\pi/2, \pi/2)$, (π, π) symmetric points of the BZ. Modeling the changes of the a, b, c lattice parameters in the GTB method with an essentially three-dimensional five-band p–d model, we reproduced the experimental three-peak structure and its concentration dependence. One may say our results indicate that the $(0, 0)$ and (π, π) peaks result from the two-hole $^3B_{1g}$ counterpart for the Zhang–Rice state near E_F, which appears at far higher binding energies in two-dimensional three-band p–d models or t–J models.

Our data also support the earlier scenario [16, 17] that the dispersion along the $(\pi/2, \pi/2) \longrightarrow (\pi, 0)$ direction is strongly reduced by the inclusion of the apical oxygen orbital, and its inclusion is absolutely essential for obtaining the weak dispersion observed experimentally. Thus, we offer a new testing ground for the theory of band structure in high-T_c cuprates.

Fig. 2. The dispersion of the top of the valence band calculated by the GTB method for different Y contents x. $Y(x)$ as indicated in the figure. The respective t_{pp} and t'_{pp} hopping parameters used for the calculations are given in table.
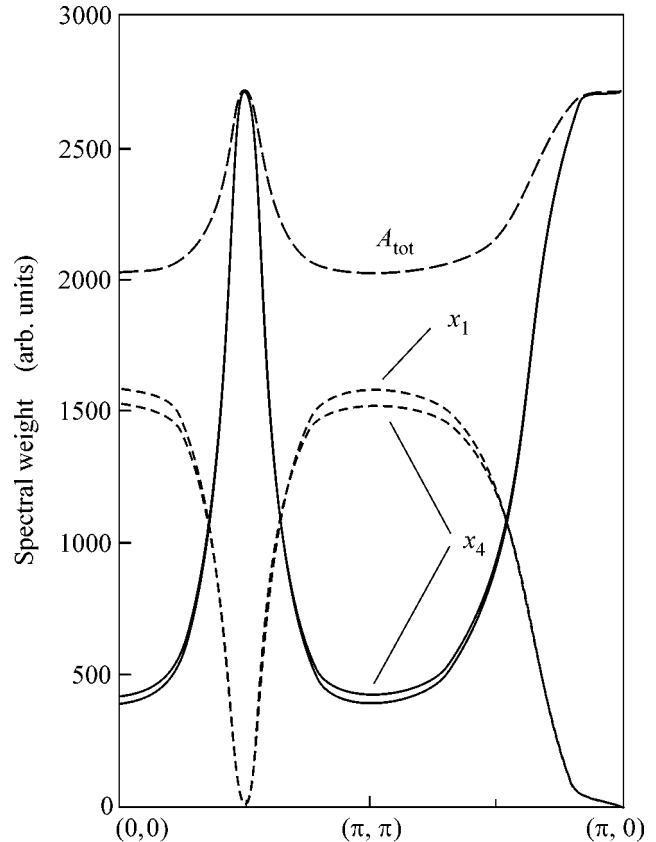
Fig. 3. Partial weights of the triplet states (dotted line) and singlet states (solid line) to A_{tot}—total spectral intensity at two different Y contents, $x_1 > x_4$. Here, the spectral function $A(\mathbf{k}, \omega)$ is taken along the peak positions in the $(\mathbf{k}, \omega)$ plane according to the dispersion shown in Fig. 1.
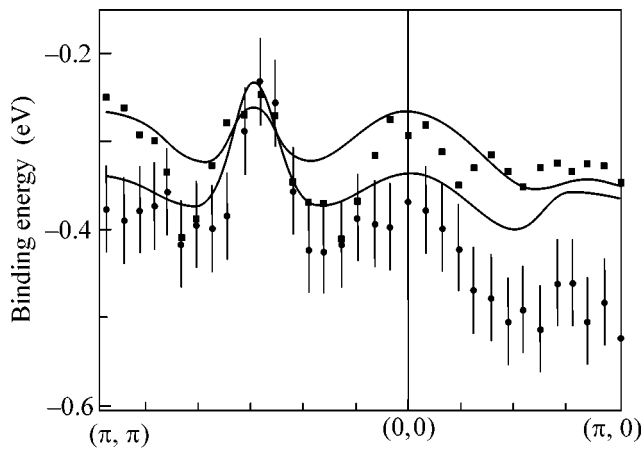
Fig. 4. Comparison of experimental (dots, $x = 0.55$; squares, $x = 0.92$) versus theoretical (dashed line, $x = x_4 = 0.55$; solid line, $x = x_1 = 0.92$ from Fig. 2) dispersions for the samples with the highest ($x = 0.92$) and lowest ($x = 0.55$) Y concentration along ΓX ($(0, 0) \longrightarrow (\pi, \pi)$). The experimental $x = 0.92$ dispersion has been shifted to obtain a common valence band maximum with the $x = 0.55$ dispersion (see also the text).

REFERENCES

1. H. Kamimura and M. Eto, J. Phys. Soc. Jpn. **59**, 3053 (1990).
2. M. Eto and H. Kamimura, Physica C (Amsterdam) **185–189**, 1599 (1991).
3. H. Eskes *et al.*, Phys. Rev. B **41**, 288 (1990).
4. V. A. Gavrichkov and S. G. Ovchinnikov, Fiz. Tverd. Tela (St. Petersburg) **40**, 184 (1998) [Phys. Solid State **40**, 163 (1998)].
5. F. Ronning *et al.*, Phys. Rev. B **67**, 035113 (2003) and references therein.
6. C. Durr *et al.*, Phys. Rev. B **63**, 014505 (2001) and references therein.
7. M. Karpinnen *et al.*, Phys. Rev. B **67**, 134522 (2003).
8. C. Janowitz *et al.*, Czech. J. Phys. **47**, 403 (1997).
9. C. Janowitz *et al.*, Physica B (Amsterdam) **259**, 1134 (1999).
10. K. Rossnagel *et al.*, Nucl. Instrum. Methods Phys. Res. A **467**, 1485 (2001).
11. D. S. Marshall *et al.*, Phys. Rev. Lett. **76**, 4841 (1996).
12. J. C. Campuzano *et al.*, Phys. Rev. Lett. **83**, 3709 (1999).
13. P. Aebi *et al.*, Phys. Rev. Lett. **72**, 2757 (1994).
14. B. O. Wells *et al.*, Phys. Rev. Lett. **74**, 964 (1995).
15. V. A. Gavrichkov *et al.*, JETP **91**, 369 (2000); Phys. Rev. B **64**, 235124 (2001).
16. J. B. Grant and A. K. McMahan, Phys. Rev. B **46**, 8440 (1992).
17. R. Raimondi *et al.*, Phys. Rev. B **53**, 8774 (1996).

Nonbonding Oxygen Holes and Spinless Scenario of Magnetic Response in Doped Cuprates¶

A. S. Moskvin

Department of Theoretical Physics, Ural State University, Yekaterinburg, 620083 Russia

Received November 2, 2004

Both theoretical considerations and experimental data point to a more complicated nature of the valence hole states in doped cuprates than is predicted by the Zhang–Rice model. Actually, we deal with a competition of a conventional hybrid Cu $3d$–O $2p$ $b_{1g} \propto d_{x^2 - y^2}$ state and purely oxygen nonbonding state with $e_u x, y \propto p_{x, y}$ symmetry. The latter reveals a nonquenched Ising-like orbital moment that gives rise to a novel spinless purely oxygen scenario of the magnetic response in doped cuprates with the oxygen localized orbital magnetic moments of the order of tenths of Bohr magneton. We consider the mechanism of $^{63, 65}$Cu–O $2p$ transferred orbital hyperfine interactions due to the mixing of the oxygen O $2p$ orbitals with Cu $3p$ semicore orbitals. Quantitative estimates point to a large magnitude of the respective contributions to both the local field and electric field gradient, and their correlated character. © *2004 MAIK "Nauka/Interperiodica"*.

PACS numbers: 74.72.–h

1. INTRODUCTION

The role played by magnetism, particularly the nature of magnetic fluctuations, is one of the central issues of high-T_c cuprate physics. Nuclear magnetic resonance (NMR) and nuclear quadrupole resonance (NQR) are believed to provide the basic experimental grounds for a spin-fluctuation mechanism of high-temperature superconductivity. It is worth noting that namely the spin-lattice relaxation rates and the Knight shift measurements by the NMR and NQR stimulated the elaboration of the well-known antiferromagnetic spin-fluctuation scenario for cuprates [1]. NMR first revealed a suppression of the low-energy magnetic excitations below what is called the spin-gap temperature. In the underdoped region, it is thought that, above T_c, a pseudogap opens up in the spin fluctuation spectrum. Since the spin-gap state is believed to be related to the pairing mechanism, a large number of experimental and theoretical studies have focused on the origin of the spin gap. Despite some criticism [2], the spin-fluctuation scenario continues to be very popular in both the NMR/NQR and the HTSC community. However, a conventional approach to the hyperfine coupling and the nuclear resonance in cuprates implies a treatment within simple models usually applied to conventional metals or vice versa to a weakly covalent and weakly correlated insulator. The magnetic response is assumed to be provided by the only contribution of the spin degrees of freedom. As in parent antiferromagnetic oxides, the Cu^{2+} center with $s = 1/2$ is considered to be a main resonating center, whereas the doped holes are considered to form a usual Fermi liquid. Meanwhile, a

hole doping in the framework of the strongly correlated scenario results in the formation of well-isolated Zhang–Rice $^1A_{1g}$ singlets. The hyperfine interactions and NMR-NQR experiments in cuprates at present are interpreted within the Shastri–Mila–Rice (SMR) spin Hamiltonian [3]. A conventional approach to the analysis of $^{63, 65}$Cu NQR/NMR experiments in hole-doped cuprates corresponds to the model of uniform lattice and indirectly implies a 100% volume fraction of the equivalent resonating nuclei.

Despite a great many experimental and theoretical papers, the nature and proper description of the magnetic correlations in cuprates is still a subject of controversy. Results of the recent NQR/NMR experiments for "classic" cuprate systems 214 and 123 together with a number of early data cast doubt on the validity of the popular concepts to be widely used as a starting point for analysis of the nuclear resonance and in a more broad sense for many other physical effects. First, it should be noticed that the $^{63, 65}$Cu NQR lines in doped cuprates are sometimes unusually inhomogeneously broadened (2–4 MHz), practically irrespective of the doping level [4–12]. Experimental Cu NQR study in $La_{2 - x}Sr_xCuO_4$ and $La_2CuO_{4 + \delta}$ has revealed two distinct Cu(2) sites (A and B) with distinguishing relaxation rates and universal difference in corresponding quadrupole frequencies. Subsequently, a precise measurement of the nuclear relaxation in $La_{2 - x}Sr_xCuO_4$ has revealed a composite structure of the separate Cu NQR lines with a strong frequency dependence of T_1^{-1} across the spectrum. Lastly, the first Cu NQR measurements have revealed either an unexpectedly small value of the asymmetry parameter η or a rather large difference of

---

¶ This article was submitted by the author in English.

η for A and B components. Haase *et al.* [13] have shown that the broadening of the Cu line in the 214 system cannot be explained by spin effects and is evidence of the orbital shift modulation of a short-length scale. The full planar oxygen spectra show a correlated modulation of the electric field gradient with the spin susceptibility. NMR spin-echo double-resonance experiments uncovered a large distribution of local magnetic fields at the planar Cu sites [14]. They found that a single fluid spin-only picture could not reproduce the experimental data.

Above, we address mainly the NMR-NQR studies; however, a close inspection of other magnetic data evidences the same controversies. The absence of an ESR signal is strong evidence that local moments in cuprates do not exist. The polarized neutron results presented by Smith *et al.* [15] have demonstrated that there is neither an elastic nor a quasi-elastic magnetic response in the normal state of nearly optimally doped $YBa_2Cu_3O_{6.95}$. Their data are inconsistent with the existence of local spin magnetic moments in the CuO_2 planes. The little scattering that they observed can be assigned to ~3% of the Cu atoms carrying a spin 1/2. They note that neither the variation in magnitude of the susceptibility in the 123 system with oxygen content nor the temperature variation is consistent with the existence of local moments. The integral intensity of the famous resonance peak in 123 cuprate does not exceed 1–2% of that for spin-wave resonance in the parent system [16]. A drastic decrease in the AF susceptibility amplitude as a function of doping is found by INS, which disagrees with NMR data and questions the role of spin fluctuations in HTSC as the magnetic fluctuations seem to vanish for samples with largest T_c [16].

Both NMR-NQR and neutron measurements cannot discriminate between the spin and orbital origin of electron magnetic moments. Thus, we cannot definitely state that current experimental data unambiguously confirm the spin nature of the magnetism in doped cuprates. Furthermore, recently, there appeared many indications of the orbital magnetism in cuprates. Possible formation of antiferromagnetism below the superconducting transition temperature was found by several experimental techniques in underdoped $YBa_2Cu_3O_{6+x}$ and $La_{2-x}Sr_xCuO_4$ [17–21]. The relatively small values of the observed magnetic moments [17–19] (0.01–0.05β_e) have indicated an orbital rather than a spin origin of the observed antiferromagnetism. The most recent ARPES observation of the circular dichroism in the normal state of underdoped and overdoped Pb-Bi2212 samples [22] also may be related to the persistent orbital currents.

The NQR study provides a more direct proof of the formation of orbital magnetism since it is performed in zero magnetic field. Thus, the internal magnetic moments, if they are present, will result in an NQR line splitting. The first experimental evidence for the formation of the internal magnetic moments in the under-

doped three-CuO_2-layer $Hg_{0.8}Cu_{0.2}Ba_2Ca_2Cu_3O_{8+\delta}$ (Hg-1223) high-T_c cuprate superconductor below $T_c = 134$ K has been presented by Breitzke *et al.* [23]. Using the NQR technique, they show that Cu NQR lines split below T_c due to a Zeeman splitting originating from the internal magnetic fields within the CuO_2 layers. These results strongly favor formation of staggered orbital currents as an origin of the observed phenomenon. The values of the internal magnetic fields vary from the inner to the outer CuO_2 layer and are on the order of several hundred gauss. Note that the fields occur below T_c and their intensities increase with decreasing temperature. The ^{199}Hg Knight shift measurements in $HgBa_2CuO_{4+\delta}$ [24] have revealed very large anisotropic shifts which are assigned to orbital magnetic moments $\mu \approx 0.04\beta_e$ localized on the oxygen positions. The $^{63,65}Cu$ shift distribution in $La_{1.85}Sr_{0.15}CuO_4$ has been found recently to be of *orbital* (!) origin [14].

In our opinion, these and many other experimental observations point to an inconsistency of a conventional model of the well-isolated spin and orbital Zhang–Rice (ZR) singlet $^1A_{1g}$ [25] believed to be a ground state of the hole-doped CuO_4 center in the CuO_2 layers. Here, it should be noted that, when speaking of a Zhang–Rice singlet as being "well isolated," one implies that the $^1A_{1g}$ ground state for the CuO_4 plaquette with the two holes of the $b_{1g}(d_{x^2-y^2})$ symmetry is well separated from any other excited two-hole states. Both, experimental data and theoretical model considerations provide evidence in favor of a more complicated structure of the valence multiplet for the hole-doped CuO_4 center rather than the simple ZR singlet, albeit the latter is a guideline in the overwhelming majority of current model approaches.

So, Yoshinari *et al.* [26] have undertaken the Cu NQR study of the isolated hole centers in $La_2Cu_{0.5}Li_{0.5}O_4$. Their results could be interpreted as convincing evidence of the singlet-triplet structure of the hole center. The authors have revealed the spin singlet ground state ($S = 0$) and the low-lying spin triplet state ($S = 1$) with the singlet-triplet separation $\Delta_{ST} = 0.13$ eV, which is comparable with the Cu–Cu nearest neighbor exchange integral in the parent oxide La_2CuO_4. An experimental indication of the appreciable role of the O $2p\pi$ orbitals in the ^{17}O hyperfine coupling was obtained by Yoshinari [27]. This implies a complicated nature of the ground-state manifold for the CuO_4 center with a significant mixing of the Zhang–Rice singlet and some other molecular term, whose symmetry should be distinct from $^1A_{1g}$. This conclusion conflicts with the widespread opinion regarding the good isolation of the Zhang–Rice singlet.

The nature of the valent hole states in doped cuprates is considered as being of great importance for the high-T_c problem. Having solved the problem, we could justify the choice of the relevant effective Hamil-

tonian together with the opportunities of a mapping to the single band t–J or Hubbard model.

Below, we show that the going beyond the ZR model does predict a novel spinless scenario of magnetic response in cuprates.

2. A–E ORBITAL STRUCTURE OF HOLE CuO_4 CENTERS IN CUPRATES

The intrinsic nature of electron and hole centers in oxides is related to the self-trapped charge transfer (CT) excitons. Both experimental observations and theoretical analysis point to a complex two-component structure of the low-energy CT band near 2 eV in parent insulating cuprates [28, 29]. Here, we deal with a superposition of rather well defined one- and two-center CT excitons. The former is associated with a dipole-allowed transition $b_{1g} \longrightarrow e_u$ from the ground state b_{1g}^b to the purely oxygen nonbonding doublet $e_u(\pi)$ in the CuO_4 plaquette, which is allowed in the "in-plane" polarization $\mathbf{E} \perp C_4$. The latter is attributed to a $b_{1g} \longrightarrow b_{1g}$ CT between two neighboring CuO_4 plaquettes with the formation of electron CuO_4^{7-} and hole CuO_4^{5-} centers. Here, the electron center nominally represents the system of Cu^{1+} and O^{2-} ions with completely filled shells, whereas the hole one represents the system with two b_{1g}^b holes forming the ZR singlet [25]. The one-center CT exciton formally consists of the conventional electron center and unconventional hole center with actually two-hole configuration $b_{1g}e_u$ resulting in a spin singlet ^1E_u or triplet term ^3E_u, respectively. Both CT excitons can interact with each other. Hence, to describe the el–h-structure of both excitons on an equal footing, one needs to consider the conventional electron center CuO_4^{7-} and unconventional CuO_4^{5-} hole center with actual $^1A_{1g}$, $^{1,3}E_u$ multiplet. Hence, unlike a simple ZR model, our model assumes a quasi-degeneracy in the ground state of the hole CuO_4^{5-} center with two close (in energy) $^1A_{1g}$ (ZR-singlet) and $^{1,3}E_u$ terms of b_{1g}^2 and $b_{1g}e_u$ configurations, respectively. This implies two nearly equivalent locations for the additional hole, either in the Cu $3d$–O $2p$ hybrid $b_{1g}(d_{x^2-y^2})$ state to form ZR singlet $^1A_{1g}$ or in a purely oxygen nonbonding doublet $e_{ux,y}$ state to form the $^{1,3}E_u$ state. The figure shows the term structure of the actual *valent A–E multiplet* for hole CuO_4^{5-} center together with the single-hole basis orbitals. These orbitals are defined as follows:

$$|b_{1g}^b\rangle = \cos\alpha_{b_{1g}}|b_{1g}(3d)\rangle + \sin\alpha_{b_{1g}}|b_{1g}(2p)\rangle, \quad (1)$$
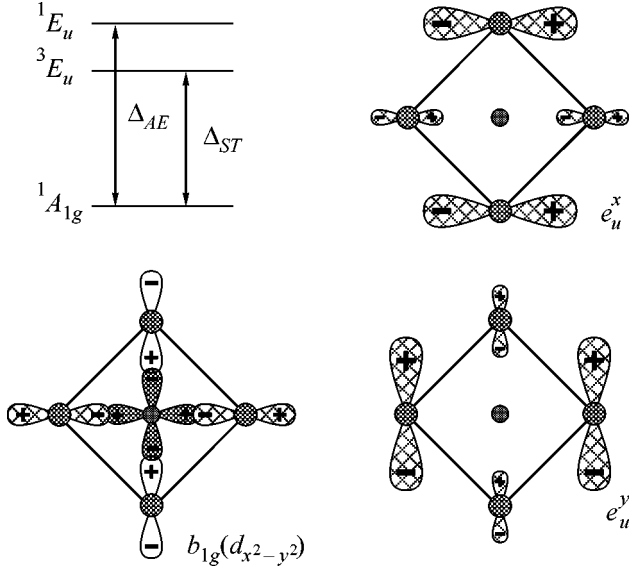
The term structure of the actual valent A–E multiplet for hole CuO_4^{5-} center together with single-hole basis b_{1g}^b and $e_{ux,y}^b$ orbitals.

where $b_{1g}(3d) = 3d_{x^2-y^2}$ and $b_{1g}(2p)$ are copper and oxygen molecular orbitals with b_{1g} symmetry. There are two types of purely oxygen nonbonding orbitals with e_u symmetry, $e_u(\sigma)$ and $e_u(\pi)$, respectively, that hybridize with each other (equally for both types (x, y) of such orbitals):

$$|e_u^b\rangle = \cos\alpha_e|e_u(\pi)\rangle + \sin\alpha_e|e_u(\sigma)\rangle;$$
$$|e_u^a\rangle = \sin\alpha_e|e_u(\pi)\rangle - \cos\alpha_e|e_u(\sigma)\rangle, \quad (2)$$

where

$$\tan 2\alpha_e = \frac{2t_{e_u}^{pp}}{\epsilon_{pe_u(\sigma)} - \epsilon_{pe_u(\pi)}}, \quad (3)$$

and

$$t_{e_u}^{pp} = -(t_{pp\sigma} + t_{pp\pi})$$

is an effective transfer integral with $t_{pp\sigma} < 0$, $t_{pp\pi} > 0$ being two types of pp transfer integrals, for σ and π bonding, respectively $\left(|t_{pp\pi}| \approx \frac{1}{2}|t_{pp\sigma}|\right)$. Hereafter, we preserve the notation $e_u(\sigma)$, $e_u(\pi)$ for dominantly σ or π orbital, respectively. Interestingly, the $e_u(\sigma)$, $e_u(\pi)$ orbitals could form two types of circular current $p_{\pm 1}$-like states: $e_{u\pm 1}(\sigma)$, $e_{u\pm 1}(\pi)$, respectively, with Ising-like orbital moment

$$\langle e_{u\pm 1}(\pi)|l_z|e_{u\pm 1}(\pi)\rangle$$
$$= -\langle e_{u\pm 1}(\sigma)|l_z|e_{u\pm 1}(\sigma)\rangle = \pm\sin 2\alpha_e \quad (4)$$

or two types of currentless $p_{x,y}$-like $e_{ux,y}(\sigma)$, $e_{ux,y}(\pi)$ states with a quenched orbital moment. The A–E model with a b_{1g}–e_u competition goes essentially beyond the well-known ZR model. In a sense, the valence $(b_{1g}^2)^1A_{1g} - (b_{1g}e_u)^{1,3}E_u$ multiplet for the hole center represents an unconventional state with Cu valence resonating between Cu^{3+} and Cu^{2+}, or "ionic-covalent" bonding. In other words, we deal with a specific version of the "correlation" polaron, introduced by Goodenough and Zhou [30], Such centers are characterized by strong coupling with the lattice and can reveal the (pseudo) Jahn–Teller effect [31].

The orbital doublet terms $^{1,3}E_u$ for hole CuO_4^{5-} center are straightforwardly derived from the two-hole $b_{1g}e_u$ configuration, whereas the configurational interaction is surely to be taken into account when deriving the ZR singlet $^1A_{1g}$. For the reasonable values of parameters (in eV) $U_d = 8.5$, $U_p = 4.0$, $V_{pd} = 1.2$, $\epsilon_d = 0$, $\epsilon_p = 3.0$, $t = 1.3$ [28], its wave function can be written as follows:

$$\Psi_1 = |ZR\rangle = -0.25|d^2\rangle + 0.95|dp\rangle - 0.19|p^2\rangle,$$

where three b_{1g}^2-like configurations are mixed. This function reflects the well-known result that the ZR-singlet represents a two-hole configuration with one predominantly Cu $3d$ and one predominantly O $2p$ hole, however, having the same b_{1g} symmetry.

The b_{1g}–e_u hole competition reflects the subtle balance between the gain in electron–electron repulsion ($U_{dd} > V_{pd}$) and the loss in one-particle energy, both affected by lattice polarization. The b_{1g}–e_u or A–E model is supported both by local-density-functional calculations [32] and by the *ab initio* unrestricted Hartree–Fock self-consistent field molecular orbital (MO) method (UHF-SCF) for copper–oxygen clusters [33, 34]. To the best of our knowledge, one of the first quantitative conclusions on a competitive role of the hybrid copper–oxygen $b_{1g}(d_{x^2-y^2})$ orbital and purely oxygen O $2p_\pi$ orbitals in the formation of valent states near the Fermi level in the CuO_2 planes has been made by McMahan *et al.* [32] and Tanaka *et al.* [33, 34]. Namely, these orbitals, as they state, define the low-energy physics of copper oxides.

In connection with the valent $^1A_{1g} - {}^{1,3}E_u$ manifold model for copper oxides, one should note and comment on the results of the paper by Tjeng *et al.* [35], where the authors state that they "are able to unravel the different spin states in the single-particle excitation spectrum of antiferromagnetic CuO and show that the top of the valence band is of pure singlet character, which provides strong support for the existence and stability of Zhang–Rice singlets in high-T_c cuprates." However, in their photoemission work, they made use of the Cu $2p_{3/2}(L_3)$ resonance condition that allows one to detect

unambiguously only copper photohole states; hence, they cannot see the purely oxygen photohole e_u states.

It is interesting to note that, among three possible states for a trapped hole in cuprate, ZR singlet $^1A_{1g}$, spin singlet ^1E_u, and spin triplet ^3E_u, only the latter provides relevant conditions for the hole transport through antiferromagnetic background. In other words, one might speak about the spin-triplet channel of $e_u(\pi)$ hole transport as a main mechanism of conductivity in insulating cuprates [36].

2.1. Unconventional Magneto-Electric CuO_4 Hole Centers beyond Simple ZR Singlet Picture

The unconventional orbital A–E structure of the hole CuO_4^{5-} center in EH droplet goes beyond the simple ZR-singlet picture and deserves closer examination. Neglecting the spin degree of freedom, we introduce a pseudospin formalism to describe the orbital states of the CuO_4 centers in the framework of the valent $(^1A_{1g}, {}^1E_u)$ multiplet model. Three orbital states of the $(^1A_{1g}, {}^1E_u)$ multiplet we associate with three states of *orbital pseudospin* $S = 1$: $|z\rangle = |^1A_{1g}\rangle$; $|x, y\rangle = |^1E_u x, y\rangle$. Then the pseudospin matrix has a very simple form: $\langle i|\hat{S}_k|j\rangle = i\epsilon_{ikj}$. A complete set of pseudospin operators should include both **S** and five spin-quadrupole operators

$$\{\widetilde{\hat{S}_i, \hat{S}_j}\} = \{\hat{S}_i, \hat{S}_j\} - \frac{2}{3}\hat{\mathbf{S}}^2\delta_{ij}.$$

These pseudospin operators are not to be confused with real physical spin operators as they act in a pseudospace. Nevertheless, all these correspond to real physical quantities. First, the z component of pseudospin defines the only nonzero z component of the Ising-like orbital magnetic moment, $\hat{\mathbf{M}} = \hat{g}^M\hat{\mathbf{S}}$, with the only nonzero g_{zz} component of the g^M tensor. Microscopically, the effective magnetic moment is generated by the orbital currents for the e_u hole. Taking into account only local oxygen contributions, one may write

$$\hat{\mathbf{M}} = \beta_e \sum_{n=1}^{4} \hat{\mathbf{l}}_n,$$

and

$$g_{zz}^M = i\beta_e\langle E_u x| \sum_{n=1}^{4} \hat{l}_{nz}|E_u y\rangle,$$

where $\hat{\mathbf{l}}_n$ is the orbital momentum operator for n-oxygen. Second, the $S_{x,y}$ pseudospin components define the unconventional quantity with spatiotransformational properties of polar vector like electric field, and time-inversion symmetry like magnetic field. This is a so-called toroidal moment which can be defined for the

CuO$_4$ plaquette as follows: $\hat{\mathbf{T}} = [\mathbf{g}^T \times \hat{\mathbf{S}}]$, where the g^T vector has the only nonzero z component. Microscopically, the effective toroidal moment can be derived through the local oxygen effective orbital moments as follows:

$$\hat{\mathbf{T}} = \beta_e \sum_{n=1}^{4} [\mathbf{R}_n \times \hat{\mathbf{l}}_n],$$

and

$$g_z^T = i\beta_e \langle A_{1g}| \sum_{n=1}^{4} R_{nx} \hat{l}_{nz} |E_u y\rangle. \quad (5)$$

It should be emphasized that both the magnetic and the toroidal moment are generated by the orbital currents for the oxygen holes. The numerical magnitude of the effective orbital magnetic moment in the E_u state is determined mainly by the mixing of O $2p\pi$ and O $2p\sigma$ orbitals (see Eqs. (2) and (3))

$$g_{zz}^M = \beta_e \sin 2\alpha_e,$$

where $\sin\alpha_e$ is a covalency parameter for $e_u(\pi) - e_u(\sigma)$ bond. For a relatively small π–σ mixing,

$$g_{zz}^M \approx \beta_e \tan 2\alpha_e = \frac{2\beta_e t_{e_u}^{pp}}{\epsilon_{pe_u(\sigma)} - \epsilon_{pe_u(\pi)}} \approx 0.2\beta_e$$

given the reasonable values $t_{e_u}^{pp} \approx 0.3$ eV and $|\epsilon_{pe_u(\sigma)} - \epsilon_{pe_u(\pi)}| \approx 3.0$ eV. For the g^T vector, we readily obtain

$$g_z^T = \frac{1}{\sqrt{2}} \beta_e R_{\mathrm{CuO}} \cos\alpha_e \sin\alpha_{b_{1g}},$$

where $\sin\alpha_{b_{1g}}$ is a covalency parameter for $b_{1g}(3d) - b_{1g}(2p)$ bond. This expression together with (5) implies that the toroidal moment is generated by oxygen orbital moments

$$l_z = \frac{1}{2\sqrt{2}} \beta_e \cos\alpha_e \sin\alpha_{b_{1g}},$$

whose value can be estimated to be of the order of $0.2\beta_e$ given $|\sin\alpha_{b_{1g}}| \approx 0.6$. It is quite probable that the toroidal fluctuations will be comparable to or even more pronounced than that of a conventional magnetic moment. The toroidal moment is distributed on the CuO$_4$ plaquette and produces a nonzero dipole magnetic field. For all points lying in the CuO$_4$ plane, the field has c-axis orientation, whereas it has ab orientation for all points lying in other symmetry planes.

Above, we estimated the maximal values of magnetic and toroidal moments for the A–E model of CuO$_4$ center. Puzzlingly, these compete with Cu^{2+} spin magnetic moments in parent oxides, which are markedly reduced by a quantum reduction and covalent effects.

Actually, we should deal with the quenching effect of "single-ion" anisotropy or other crystalline fields on the orbital magnetism.

The symmetric quadratic pseudospin operators define effective electric dipole and quadrupole moments. The former has a planar character with two nonzero components: $\hat{d}_x = d_0\{\hat{S}_x\hat{S}_z\}$, $\hat{d}_y = d_0\{\hat{S}_y\hat{S}_z\}$, where d_0 is the effective dipole moment length. The latter has three nonzero components $\hat{Q}_{A_1} = Q_{A_1}\left(\hat{S}_z^2 - \frac{2}{3}\right)$, $\hat{Q}_{B_1} = Q_{B_1}(\hat{S}_x^2 - \hat{S}_y^2)$, $\hat{Q}_{B_2} = Q_{B_2}\{\hat{S}_x\hat{S}_y\}$ with three quadrupole parameters Q_Γ. Thus, the CuO$_4$ plaquette with ($^1A_{1g}$, ^1E_u) valent multiplet forms an unconventional magneto-electric center characterized by eight independent orbital order parameters. Generally speaking, our model represents a theory that predicts broken time-reversal (T) symmetry, two-dimensional parity (P), and basic tetragonal symmetry.

2.2. Oxygen Holes and Orbital Hyperfine Interactions beyond the Shastry–Mila–Rice Model

Below, we address some unconventional properties of $^{63,\,65}$Cu hyperfine interactions for the spin-singlet $^1A_{1g} - {}^1E_u$ valence multiplet of the CuO$_4$ center resulting from its nonquenched orbital moment.

The nuclear resonance experiments at present are interpreted within the Shastri–Mila–Rice spin-Hamiltonian [3]

$$\hat{H}_{hf} = \sum_{mn} {}^{63}\mathbf{I}(n)[\hat{A}(n)\mathbf{s}(n) + B)(nm)\mathbf{s}(m)], \quad (6)$$

based on the assumption that the spin density in the CuO$_4$ centers is localized on the copper ions. Here, $\hat{A}(n)$ is the hyperfine tensor for the direct, on-site coupling of the $^{63,\,65}$Cu nuclei to the Cu^{2+} spins ($s = 1/2$), and B (nm) is the strength of the transferred hyperfine coupling of the $^{63,\,65}$Cu nuclear spin to the four nearest neighbor Cu^{2+} spins.

The effective Hamiltonian of nuclear quadrupole interactions for $^{63,\,65}$Cu nuclei has a conventional form as follows:

$$\hat{H}_Q = \frac{Q}{4I(2I-1)}[V_{zz}(3\hat{I}_z^2 - \hat{\mathbf{I}}^2) + \eta V_{zz}(\hat{I}_x^2 - \hat{I}_y^2) + \epsilon V_{zz}(\hat{I}_x\hat{I}_y + \hat{I}_y\hat{I}_x)], \quad (7)$$

where for the CuO$_4$ center

$$V_{zz} = V_{zz}(\mathbf{R}) = (V_{zz}^E - V_{zz}^A + V_{zz}^p)\langle \hat{S}_z^2\rangle_{\mathbf{R}} + V_{zz}^A,$$

$$\eta V_{zz} = 3V_{zz}^p\langle \hat{S}_x^2 - \hat{S}_y^2\rangle_{\mathbf{R}}, \quad \epsilon V_{zz} = 3V_{zz}^p\langle\{\hat{S}_x, \hat{S}_y\}\rangle_{\mathbf{R}},$$

where **R** is the radius vector of the CuO$_4$ center. Parameters V_{zz}^A and V_{zz}^E determine the b_{1g} contribution to V_{zz} for $^1A_{1g}$ and ^1E_u terms, respectively, while V_{zz}^p determines the total contribution of the Cu p electrons. The $^{63,\,65}$Cu NQR frequency can be written as follows:

$$\nu_Q = \frac{1}{2}|QV_{zz}|\sqrt{1 + \frac{1}{3}(\eta^2 + \epsilon^2)}.$$

A variety of model EFG calculations were carried out [37–40]. First, we would like to note the extreme sensitivity of the EFG to the calculated anisotropic charge distribution of the semicore Cu $3p$ states, which are characterized by the very large magnitude of the effective quadrupole parameter $\langle 1/r^3 \rangle_{3p} \simeq 150$ [37], or 170 a.u. [39]. This parameter governs the magnitude of both the EFG tensor and the local magnetic field induced by a Cu $3p$ electron on the copper nucleus:

$$V_{ij} = -\frac{2e}{5}\langle 1/r^3 \rangle_{3p}\langle(\widetilde{3\hat{l}_i\hat{l}_j} - 2\delta_{ij})\rangle; \quad (8)$$

$$\mathbf{H}_{loc} = -2\beta_e\langle 1/r^3 \rangle_{3p}\mathbf{l}, \quad (9)$$

where **l** is an orbital momentum for the Cu $3p$ electron, and $\widetilde{\hat{l}_i\hat{l}_j} = 1/2(\hat{l}_i\hat{l}_j + \hat{l}_j\hat{l}_i)$. Thus, the Cu $3p$ contribution to the EFG and to the local field can reach colossal values such as 100 (in 10^{22} V m^{-2}) and 10^3 T, respectively. In conventional cuprate scenarios with valence $b_{1g} \propto d_{x^2-y^2}$ holes, there is no hybridization between Cu $3p$ and valence states, and the semicore Cu $3p$ contribution to electric and magnetic hyperfine interactions can be taken into account in frames of Sternheimer shielding–antishielding effects. However, the semicore Cu $3p$ role becomes of particular significance for the $^1A_{1g}$, ^1E_u valence multiplet of electron and hole centers with varying hole density in oxygen e_u states which have the same symmetry as Cu $3p_{x,\,y}$ states; that is, these can hybridize with each other. As a result, the purely oxygen e_u orbital turns into O $2p$–Cu $3p$ hybrid MO

$$\phi_{x,\,y}^{e_u} \longrightarrow \Phi_{x,\,y}^{e_u} = c_{2p}\phi_{x,\,y}^{e_u} + c_{3p}\phi_{x,\,y}^{3p}$$

with MO coefficients $c_{3p} \ll c_{2p}$. Thus, we arrive at the effective magnetic and electric "oxygen-to-copper" transferred orbital hyperfine interaction. The effective $e_u(\pi)$ contribution to the local field on the copper nucleus can be written in terms of pseudospin formalism as (in tesla)

$$H_{loc}^z = -2\beta_e\langle 1/r^3 \rangle_{3p}|c_{3p}(\pi)|^2\langle S_z \rangle$$
$$\approx 2.0 \times 10^3 |c_{3p}(\pi)|^2\langle S_z \rangle \quad (10)$$

irrespective of the magnitude of the orbital moment for the CuO$_4$ center. For the nonzero EFG components V_{zz}, V_{xx}, V_{yy}, V_{xy}, we obtain (in 10^{22} V m^{-2})

$$V_{ij} = -\frac{2e}{5}\langle 1/r^3 \rangle_{3p}|c_{3p}(\pi)|^2\langle(\widetilde{3\hat{S}_i\hat{S}_j} - 2\delta_{ij})\rangle$$
$$\approx 2.7 \times 10^2|c_{3p}(\pi)|^2\langle(\widetilde{3\hat{S}_i\hat{S}_j} - 2\delta_{ij})\rangle. \quad (11)$$

Interestingly, Eqs. (10) and (11) imply that the ratio between the local field and EFG is governed only by the ratio between respective pseudospin averages:

$$H_{loc}^z : V_{ij} = \beta_e\langle S_z \rangle : \frac{e}{5}\langle(\widetilde{3\hat{S}_i\hat{S}_j} - 2\delta_{ij})\rangle. \quad (12)$$

The simple relation between the local field and EFG governed only by the respective pseudospin averages implies a rather subtle interplay between magnetic and electric contributions both to NMR-NQR frequencies and to the spin-lattice relaxation rate for copper nuclei. The numerical calculations allow us to expect the O $2p$–Cu $3p$ mixing coefficient c_{3p} to be of the order of several hundredths. Indeed, the overlap contribution to this coefficient given the Cu–O separations $R_{CuO} \approx$ 1.9 Å is estimated [41] to be $c_{3p}(overlap) = S_{Cu3p-O2p}^\sigma \approx$ –0.05 for the strongest Cu $3p$–O $2p$ σ-bonding and $S_{Cu3p-O2p}^\pi \approx -0.5 S_{Cu3p-O2p}^\sigma$. In such a way, the oxygen $e_u(\pi)$ hole contribution to the orbital hyperfine interactions due to the Cu $3p\pi$–O $2p\pi$ overlap can be estimated as $|H_{loc}| \le 1$ tesla and $|V_{ij}| \le 0.3 \times 10^{22}$ V m^{-2} for magnetic and electric terms, respectively. It should be noted that the respective maximal values correspond to a very large magnitude of effective NMR and NQR frequencies of the order of 10 MHz. Moreover, the oxygen $e_u(\sigma)$ hole contribution can be approximately four times bigger.

3. CONCLUSIONS

We showed that, going beyond a simple ZR model, we arrive at a complex $^1A_{1g}-^{1,\,3}E_u$ structure of the valent multiplet for the hole CuO$_4^{5-}$ center in cuprate with engaging orbital degree of freedom. Moreover, it should be emphasized that the simple $^1A_{1g}-^1E_u$ model implies a spinless purely orbital and purely oxygen scenario of magnetic response and hyperfine interactions in doped cuprates. However, we do not completely reject the spin degree of freedom. Indeed, our model implies a near degeneracy for singlet ^1E_u and triplet ^3E_u terms with many interesting manifestations of the spin singlet-triplet magnetism [42]. Moreover, both spin and orbital degrees of freedom are likely to be involved in formation of the complex magnetic response of doped cuprates with a relative weight that manifests itself diversely depending on the energy range and experimental conditions (NMR-NQR, magnetic susceptibility, magnetic neutron scattering, etc.).

REFERENCES

1. A. J. Millis, H. Monien, and D. Pines, Phys. Rev. B **42**, 167 (1990).

2. P. W. Anderson, Adv. Phys. **46**, 3 (1997).

3. B. Shastry, Phys. Rev. Lett. **63**, 1288 (1989); F. Mila and T. M. Rice, Physica C (Amsterdam) **157**, 561 (1989).

4. T. Tsuda, T. Shimizu, H. Yasuoka, *et al.*, J. Phys. Soc. Jpn. **57**, 2908 (1988).

5. S. Fujiyama, Y. Itoh, H. Yasuoka, and Y. Ueda, J. Phys. Soc. Jpn. **57**, 2908 (1988).

6. Y.-Q. Song, M. A. Kennard, M. Lee, *et al.*, Phys. Rev. B **44**, 7159 (1991).

7. T. Imai, C. P. Slichter, K. Yoshimura, and K. Kosuge, Phys. Rev. Lett. **70**, 1002 (1993).

8. P. C. Hammel, A. P. Reyes, S.-W. Cheong, *et al.*, Phys. Rev. Lett. **71**, 440 (1993).

9. T. Goto, S. Kazama, and T. Fukase, Physica C (Amsterdam) **235–240**, 1661 (1994).

10. R. L. Martin, Phys. Rev. Lett. **75**, 744 (1995).

11. Y. Itoh, M. Matsumura, and H. Yamagata, J. Phys. Soc. Jpn. **65**, 3747 (1996).

12. A. A. Gippius, E. V. Antipov, W. Hoffmann, and K. Lueders, Physica C (Amsterdam) **276**, 57 (1997).

13. J. Haase, C. P. Slichter, and C. T. Milling, J. Supercond. **15**, 339 (2002).

14. J. Haase, C. P. Slichter, R. Stern, *et al.*, J. Supercond. **13**, 723 (2000).

15. T. J. Smith, K. H. Andersen, U. Beck, *et al.*, J. Magn. Magn. Mater. **177–181**, 543 (1998).

16. P. Bourges, cond-mat/0009373.

17. H. A. Mook, Pengcheng Dai, and F. Dogan, cond-mat/0102047; Phys. Rev. B **64**, 012502-1 (2001).

18. H. A. Mook, Pengcheng Dai, S. M. Hayden, *et al.*, cond-mat/0204002.

19. Y. Sidis, C. Ulrich, P. Bourges, *et al.*, Phys. Rev. Lett. **86**, 4100 (2001).

20. J. E. Sonier *et al.*, Science **292**, 1692 (2001); R. I. Miller *et al.*, Phys. Rev. Lett. **88**, 137002 (2002).

21. B. Lake *et al.*, Science **291**, 1759 (2001).

22. S. V. Borisenko *et al.*, Phys. Rev. B **69**, 224509 (2004).

23. H. Breitzke, I. Eremin, D. Manske, *et al.*, cond-mat/0210652.

24. B. J. Suh, F. Borsa, Ming Xu, *et al.*, Phys. Rev. B **50**, 651 (1994).

25. F. C. Zhang and T. M. Rice, Phys. Rev. B **37**, 3759 (1988).

26. Y. Yoshinari, P. C. Hammel, J. A. Martindale, *et al.*, Phys. Rev. Lett. **77**, 2069 (1996).

27. Y. Yoshinari, Physica C (Amsterdam) **276**, 147 (1997).

28. A. S. Moskvin, R. Neudert, M. Knupfer, *et al.*, Phys. Rev. B **65**, 180512(R) (2002).

29. A. S. Moskvin, J. Málek, M. Knupfer, *et al.*, Phys. Rev. Lett. **91**, 037001 (2003).

30. J. B. Goodenough and J.-S. Zhou, Phys. Rev. B **49**, 4251 (1994).

31. A. S. Moskvin and Yu. D. Panov, JETP **84**, 354 (1997); Phys. Status Solidi B **212**, 141 (1999); J. Phys. Chem. Solids **60**, 607 (1999).

32. A. K. McMahan, R. M. Martin, and S. Satpathy, Phys. Rev. B **38**, 6650 (1988).

33. Jiro Tanaka, Koji Kamiya, and Chizuko Tanaka, Physica C (Amsterdam) **61**, 451 (1989).

34. J. Tanaka and C. Tanaka, J. Phys. Chem. Solids **59**, 1861 (1998).

35. L. H. Tjeng, B. Sinkovic, N. B. Brookes, *et al.*, Phys. Rev. Lett. **78**, 1126 (1997).

36. A. S. Moskvin and Yu. D. Panov, cond-mat/0008035; Solid State Commun. **122**, 253 (2002).

37. J. Yu, A. J. Freeman, R. Podloucky, *et al.*, Phys. Rev. B **43**, 532 (1991).

38. M. V. Eremin and O. V. Lavizina, Zh. Éksp. Teor. Fiz. **111**, 144 (1997) [JETP **84**, 80 (1997)].

39. P. Husser, E. Stoll, H. U. Suter, and P. F. Meier, Physica C (Amsterdam) **294**, 217 (1998); P. Husser, H. U. Suter, E. Stoll, and P. F. Meier, Phys. Rev. B **61**, 1567 (2000).

40. I. Kupcic, S. Barisic, and E. Tutis, Phys. Rev. B **57**, 8590 (1998).

41. M. V. Eremin, private communication.

42. A. S. Moskvin and A. S. Ovchinnikov, J. Magn. Magn. Mater. **186**, 288 (1998); Physica C (Amsterdam) **296**, 250 (1998).

Amorphization of Cuprite, Cu₂O, due to Chemical Decomposition under High Pressure¶

V. V. Sinitsyn[1], V. P. Dmitriev[2], I. K. Bdikin[1], D. Machon[2], L. Dubrovinsky[3], E. G. Ponyatovsky[1], and H.-P. Weber[4]

[1] *Institute of Solid State Physics, Russian Academy of Sciences, Chernogolovka, Moscow region, 142432 Russia*
e-mail: sinitsyn@issp.ac.ru
[2] *Group "Structure of Materials under Extreme Conditions," Swiss–Norwegian Beam Lines at ESRF,*
F-38043 Grenoble, France
[3] *Bayerisches Geoinstitut, Universität Bayreuth, D-95440 Bayreuth, Germany*
[4] *LCr/IPMC/FSB, Swiss Federal Institute of Technology, CH-1015 Lausanne, Switzerland*
Received November 3, 2004

Using synchrotron radiation and a diamond-anvil cell, a structural study of the phase transformations in Cu_2O is carried out from diffraction data obtained *in situ* while heating at a pressure of 30 GPa. Around 140°C, we observe a transition of Cu_2O to an amorphous state, with the amorphous state persisting to about 260°C. Further heating up to 400°C yields at first a nanocrystalline two-phase mixture of $Cu + CuO$ and, then, with prolonged heating at 400°C, full crystallization of this mixture. The present structural data are the first experimental evidence of solid-state amorphization under high pressure as an intermediate stage of the high-pressure decomposition of complex compounds. © 2004 MAIK "Nauka/Interperiodica".

PACS numbers: 74.50.+r; 74.80.Fp

One of the topical fields in present high-pressure research is the study of amorphization occurring in initially crystalline substances. More than a hundred substances have been found to undergo solid-state amorphization (SSA) due to an appropriate thermobaric treatment [1, 2]. Normally, SSA is observed in substances with two polymorphic modifications of considerably different density in their equilibrium $T–P$ phase diagrams. The transition to the amorphous state takes place either in the low-density phase upon compression or in the high-density phase upon decompression. Therefore, SSA is often considered as an intermediate stage of a "frozen" polymorphic transition. Several papers [2–4], however, have been reported where another SSA mechanism was proposed, namely, that SSA resulted from slow decomposition of a chemically pure initial crystalline phase into two crystalline phases of other composition. Typical compounds where this effect is assumed include hydroxides such as $Ca(OH)_2$ and $Ni(OH)_2$ [2], rare-earth molybdates [3], as well as many minerals that are Earth core and mantle components and have complex chemical formulas [4]. In some substances, the decomposition processes result in a considerable volume decrease, which has led Meade and Jeanloz [5] to suggest that these processes might play an important role in triggering earthquakes. Unquestionably, a clarification of the physical processes of SSA and of mineral formation in the Earth's

interior is important. An experimental study of the transition sequence *pure crystalline compound ⟶ amorphous state ⟶ crystalline products of decomposition* has so far not been carried out *in situ*, and this study, where we report on the first experimental observation of amorphization due to decomposition under pressure, fills this gap.

To study the process experimentally, we chose cuprous oxide, Cu_2O. That Cu_2O decomposes under high pressure has been recognized previously [6]. The $Cu_2O–Cu + CuO$ equilibrium line has been calculated, and the kinetic $T–P$-diagram has been plotted experimentally, including the $Cu_2O ⟶ Cu + CuO$ decomposition line on compression and the reverse synthesis line, $Cu + CuO ⟶ Cu_2O$, on decompression [6]. The equilibrium pressure at 20°C is $P = 4$ GPa, and the slope of the equilibrium line is $dT/dP = 250$ K/GPa. At $T = 350$°C, Cu_2O decomposes around $P = 7$ GPa. At higher pressures, the decomposition temperature decreases, but the slope of the decomposition line becomes less at $P > 8$ GPa, so that the decomposition temperature is about 120°C at the limit of the investigated pressure range, 10 GPa [6, 7]. Using thermobaric quenching experiments, it was found that Cu_2O under p, T conditions close to the decomposition line underwent a transition to the nanocrystalline state [7]. It is reasonable to assume therefore that all stages of decomposition, Cu_2O amorphization included, can be observed at higher pressures and lower temperatures


¶ This article was submitted by the authors in English.

when the diffusion of the decomposition products becomes slow.

The structural studies were performed at the Swiss–Norwegian beam lines (BM1A) at the European Synchrotron Radiation Facility (ESRF, Grenoble, France) by angle-dispersive diffraction techniques using monochromatic radiation (λ = 0.7109 Å). Diffraction patterns were collected with an image plate detector (MAR345). The sample-to-detector distance and the image plate inclination angles were precisely calibrated using a silicon standard. The two-dimensional diffraction images were analyzed using ESRF Fit2D software, yielding one-dimensional intensity vs. diffraction angle 2θ patterns [8].

In the experiment, pressure was increased to 30 GPa at room temperature in steps of about 10 GPa. The sample was maintained in each step for an hour in order to allow relaxation of the shear stress arising in the process of loading. Around 11 GPa, we observed a phase transition to a hexagonal phase II described earlier [9]. A further increase in pressure to 21 GPa resulted in a new diffraction pattern, indicative of a phase transition to a new crystalline modification, phase III. This phase remained upon a further pressure increase to 30 GPa, the maximum pressure applied. The analysis of the peak positions demonstrated that the reflections of phase III were well described within a simple hexagonal lattice with lattice parameters of a = 5.86 Å and c = 18.78 Å. This structure is rather different from the hexagonal $CdCl_2$-type reported earlier [9] in the same pressure range. We chose a different unit cell because additional reflections were observed. Taking these reflections into account, the a lattice parameter should be about doubled compared to the earlier data [9]. Note that the line of the $Cu_2O \rightleftharpoons Cu + CuO$ chemical equilibrium at room temperature is within the pressure range of 4 to 5 GPa; therefore, the Cu_2O phase state is out of its stability range at P > 5 GPa. It is known that the features of the phase state formed in the region of its metastability may depend on the conditions of the thermobaric loading, that is, on hydrostaticity, on the initial grain size, on the compression rate, etc. Therefore, the difference in the structures observed here and in [9] can be due to different experimental conditions on compression.

At a pressure of 30 GPa, the sample was heated to 400°C in steps of 20 to 40°C, and diffraction patterns were measured at each step. Figure 1 shows representative diffraction patterns collected upon heating. Heating results in strong broadening of all phase III reflections, with two broad halos observed at a temperature of about 140°C (curve 2 in Fig. 1). The halos indicate sample amorphization; note that the maxima of the halos lie at positions different than the positions of the strongest reflections of the hexagonal phase. It can therefore be assumed that the short-range order of the amorphous phase differs from that of phase III.
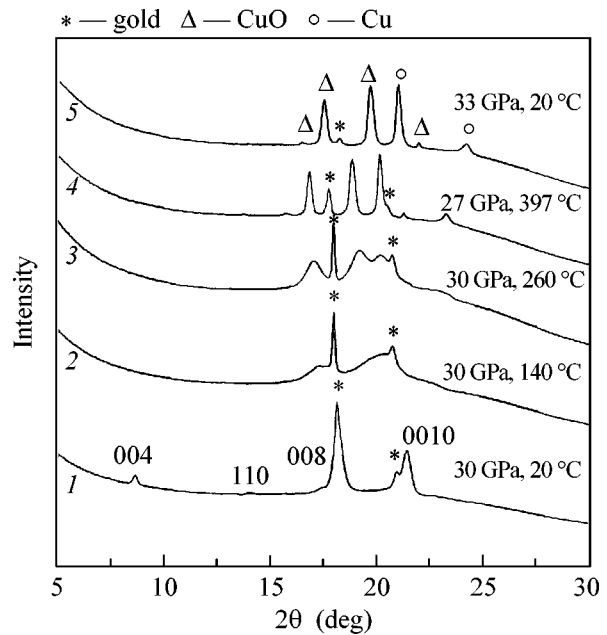
Fig. 1. The diffraction patterns of Cu_2O at $P \approx 30$ GPa and different temperatures. The (*hkl*) indices are shown for the high-pressure hexagonal phase.

A further increase in temperature leads to a gradual increase in the intensity of the first maximum, while its width decreases. At temperatures of 240 to 260°C and above, the second maximum splits into two broad peaks with nearly the same intensities (Fig. 1, curve 3). The emergence of peaks of lower intensity indicates onset of the recrystallization process. An estimation of the grain size from the half-width of the first maximum gives a value of about 6.5 nm, which is characteristic of the nanocrystalline state. The diffraction pattern demonstrates only quantitative changes in the temperature range of 240 to ~350°C, that is, decreasing width of the sample reflections and their increase in intensity with respect to the lines of gold. The widths of the sample and gold reflections become comparable at T = 400°C (Fig. 1, curve 4), which is evidence that the recrystallization process is complete. It is worth noting that the diameter of the gasket hole increases as temperature is increased, and, as a consequence, pressure in the cell somewhat decreases. To compensate this effect, we increased the load applied to the diamonds in the process of heating. This procedure, however, becomes rather complicated at high temperatures; therefore, the 400°C diffraction pattern was recorded at a somewhat lower pressure value, P = 27 GPa.
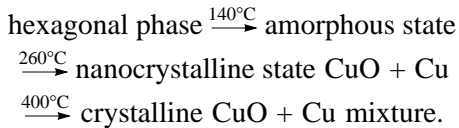
The diffraction pattern remained the same upon cooling to room temperature followed by decompression, but for the shift of all x-ray lines. The x-ray analysis at atmospheric pressure demonstrated that the recrystallized mixture consisted of CuO and Cu. Neither substance undergoes phase transitions in the T–P region of the study [10, 11]; therefore, the essentially invariable diffraction pattern on cooling and decom-
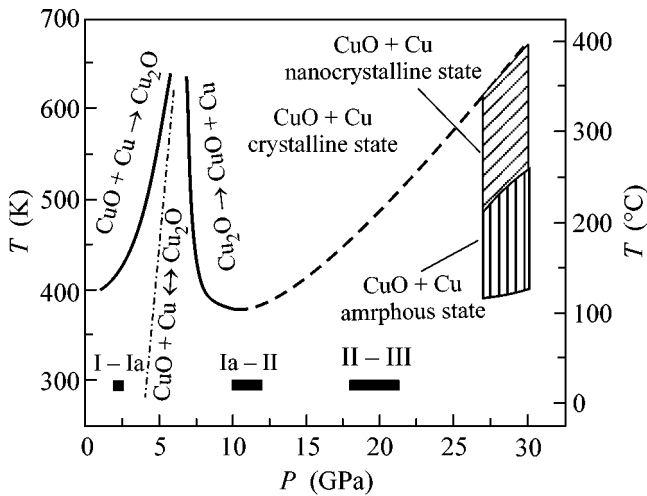
Fig. 2. The *P–T* phase diagram of Cu_2O in stable and metastable regions. The details are given in the text.

pression is reasonable. The positions of the copper and copper oxide peaks after cooling the high-pressure cell are indicated in Fig. 1 (curve *5*) (pressure increased to *P* = 33 GPa in the cooling run).

So, the following sequence of phase transformations is observed in Cu_2O in the present experiment at a pressure of 30 GPa during heating:

$$\text{hexagonal phase} \xrightarrow{140°C} \text{amorphous state}$$
$$\xrightarrow{260°C} \text{nanocrystalline state CuO + Cu}$$
$$\xrightarrow{400°C} \text{crystalline CuO + Cu mixture.}$$

The behavior of the diffraction spectrum at $T \geq 140°C$ suggests that both amorphous and, particularly, nanocrystalline states are formed as the products of the chemical decomposition reaction, $Cu_2O \longrightarrow CuO + Cu$. At low temperatures, Cu_2O decomposition is limited to a break of the chemical short-range order, resulting in amorphization. At $T \geq 260–260°C$, nanocrystalline Cu and CuO nuclei begin growing. It is not unlikely that there is some temperature interval where one of the components recrystallizes and the other component stays amorphous, due to different diffusion mobilities of the components. This interval, however, appears to be narrow at 30 GPa because both components recrystallized simultaneously at the temperature variation steps of 20 to 40°C.

Comparison of the present data and those from [6, 7, 9, 12, 13] results in the Cu_2O *T–P* phase diagram outlined in Fig. 2. The solid lines in Fig. 2 represent the kinetic lines of the $Cu_2O \longrightarrow CuO + Cu$ decomposition and $CuO + Cu \longrightarrow Cu_2O$ synthesis, and the dashed line corresponds to the line of the $Cu_2O–CuO + Cu$ equilibrium calculated earlier [6, 7]. The equilibrium line divides the *P–T* plane into two regions: the region of thermodynamic stability of the Cu_2O compound is on the left of the line, and the region of the CuO + Cu two-phase states is on the right. One structural phase transi-

tion, *cubic* (I)–*tetragonal* (Ia), concomitant with a small volume change, has been observed in the Cu_2O stability region [11]. The kinetic decomposition line is in the range between 120 and 150°C at $P \geq 8$ GPa; therefore, the Cu_2O compound can remain in the metastable state at room temperature well above the equilibrium pressure. In the Cu_2O metastable region, two phase transitions, Ia–II and II–III, take place at pressures of 10–12 GPa [7, 8] and ~18–21 GPa [8], respectively; they were also observed in the present experiment. The earlier decomposition curve has not been determined at pressures above 10 GPa, but our data show that the temperature for decomposition into crystalline states at pressures of 27–30 GPa is in the interval 390–400°C. An increase in the decomposition temperature is therefore expected at $P \geq 10$ GPa, as shown tentatively with the dashed line in Fig. 2. The region of the nanocrystalline states is in the close vicinity of the decomposition curve, whereas the region of the amorphous states is extended to lower temperatures. The temperature intervals of these regions are rather narrow at pressure up to 10 GPa, which prevented the amorphous phase from being observed at pressures of 10–15 GPa in the previous works [7].

REFERENCES

1. E. G. Ponyatovsky and O. I. Barkalov, Mater. Sci. Rep. **8**, 147 (1992).
2. S. M. Sharma and S. K. Sikka, Prog. Mater. Sci. **40**, 1 (1996).
3. E. G. Ponyatovsky, V. V. Sinitsyn, R. A. Dilanyan, and B. Redkin, Pis'ma Zh. Éksp. Teor. Fiz. **61**, 217 (1995) [JETP Lett. **61**, 222 (1995)].
4. A. K. Arora, Solid State Commun. **115**, 665 (2000).
5. C. Meade and R. Jeanloz, Science **252**, 68 (1991).
6. I. T. Belash, G. I. Peresada, and E. G. Ponyatovsky, Neorg. Mater. **13**, 666 (1977).
7. E. G. Ponyatovsky, G. E. Abrosimova, A. S. Aronin, *et al.*, Phys. Solid State **44**, 852 (2002).
8. A. P. Hammersley, S. O. Svensson, M. Hanfland, *et al.*, High Press. Res. **14**, 235 (1996).
9. A. Werner and H. D. Hochheimer, Phys. Rev. B **25**, 5929 (1982).
10. L. C. Bourne, P. Y. Yu. Zettl, and M. L. Cohen, Phys. Rev. B **40**, 10 973 (1989).
11. E. Yu. Tonkov, High Press. Phase Transform. **1**, 328 (1992).
12. M. Kalliomaki, V. Meisalo, and A. Laisaar, Phys. Status Solidi A **56**, K127 (1979).
13. D. Machon, V. V. Sinitsyn, V. P. Dmitriev, *et al.*, J. Phys.: Condens. Matter **15**, 7227 (2003).

Dissimilarity between Metallic-Like Transport in the Dielectric Spin Density Wave and Field-Induced Spin Density Wave States in (TMTSF)$_2$PF$_6$¶

A. V. Kornilov[1], V. M. Pudalov[1], Y. Kitaoka[2], K. Ishida[2], T. Mito[2], N. Tateiwa[3], T. C. Kobayashi[3], and J. S. Qualls[4]

[1] Lebedev Physics Institute, Russian Academy of Sciences, Moscow, 119991 Russia
e-mail: pudalov@lebedev.ru
[2] Division of Material Physics, School of Engineering Science, Osaka University, 560-8531 Osaka, Japan
[3] Research Center for Materials Science at Extreme Condition, Osaka University, 560-8531 Osaka, Japan
[4] Wake Forest University, Winston-Salem, NC 27109, USA
Received November 4, 2004

We report similarities and differences of the transport features in the spin density wave (SDW) and in the field-induced SDW (FISDW) phases of the quasi-one-dimensional compound (TMTSF)$_2$PF$_6$. As temperature decreases below ≈2 K, the resistance in both phases exhibits a maximum and a subsequent strong drop. However, the characteristic temperature of the $R(T)$ maximum and its scaling behavior in different magnetic fields B are evidence that the nonmonotonic $R(T)$ dependences have different origin in SDW and FISDW regions of the phase diagram. We also found that the borderline $T_0(B, P)$ which divides the FISDW region of the P–B–T phase diagram into the hysteresis and nonhysteresis domains terminates in the $N = 1$ subphase; the borderline thus has no extension to the SDW $N = 0$ phase. © 2004 MAIK "Nauka/Interperiodica".

PACS numbers: 72.15.Gd; 74.70.Kn; 75.30.Fv

The quasi-one-dimensional organic compound (TMTSF)$_2$PF$_6$ undergoes a phase transition from a metallic to spin density wave (SDW) state as temperature decreases below $T_{SDW} \approx 12$ K (at ambient pressure) [1, 2]. As pressure increases, T_{SDW} decreases and vanishes at $P = 6$ kbar [1, 2]. Application of the magnetic field B along the least conducting direction z (crystal axis c^*) restores the dielectric state; this takes place via a cascade of the field-induced spin density wave states (FISDW) accompanied by a sequence of quantum Hall effect (QHE) states with various numbers N of filled Landau bands [3–5]. A typical phase diagram of the FISDW states for $P = 7$ kbar is illustrated in the inset to Fig. 1.

Earlier [6], we found that there is another boundary, $T_0(B)$, which subdivides the field of existence of the FISDW states (at $N \neq 0$) into the low-temperature and the high-temperature domain (see the inset to Fig. 1). In the low-T domain, transitions between different FISDW states ($N \Leftrightarrow N - 1$) take place as first-order phase transitions, as the magnetic field drives the system through the FISDW phases. In the high-T domain, the transitions between different phases have a cross-over character. The above picture is consistent with a theoretical model recently suggested by Lebed [7] in which the low-T and the high-T domain have a meaning

of the quantum and the semiclassical region, respectively. The nesting vector is predicted to be partially quantized in the quantum domain and is not quantized in the semiclassical domain.

We also reported [6] that a qualitative difference between the two domains exists through the overall area of the FISDW phase. Specifically, the temperature dependence of the resistance $R(T)$ measured along the most conducting direction x (i.e., the crystal axis a) has a maximum in the vicinity of the same $T_0(B)$ line (see Fig. 1); this coincidence was observed for different pressure values from 7 to 14 kbar.

The maxima in $R_{max}(T)$ were observed earlier [8] in the $N \neq 0$ phases and have been associated with the onset of the quantum Hall effect [8–10]. Indeed, as T decreases, the Hall component of the conductivity σ_{xy} grows to the quantized value, $\sigma_{xy} \longrightarrow Ne^2/h$. As a result of the interplay between the diagonal and off-diagonal components of conductivity, R_{xx} exhibits a maximum, as follows from the equation

$$R_{xx} = \frac{\sigma_{yy}}{\sigma_{xx}\sigma_{yy} + \sigma_{xy}^2}. \tag{1}$$

Within such an explanation (see, e.g., [8, 9] and references therein), the $R(T)$ maxima are associated with the QHE and do exist in all phases with $N \geq 1$; obviously, such maxima should be missing in the dielectric SDW

¶ This article was submitted by the authors in English.
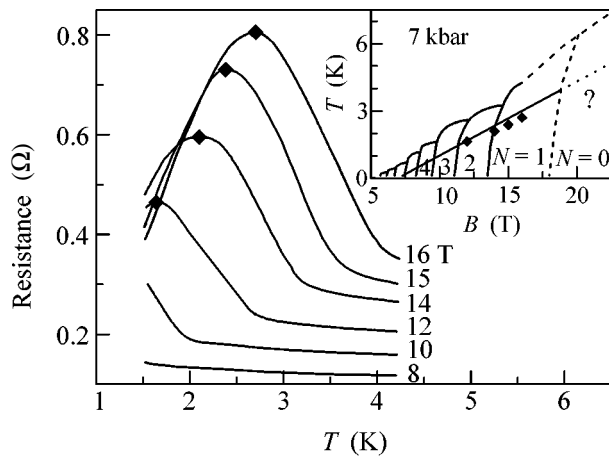
Fig. 1. Typical temperature dependence of the resistance at $P = 7$ kbar in the FISDW regime for six different values of B. Inset shows the $B–T$ phase diagram: solid curves represent the results from [6], dashed lines show the phase boundaries anticipated at higher fields according to [4, 5]. N values denote the subphase number. The thick straight line $T_0(B)$ separates the hysteresis and nonhysteresis regimes; the dotted line is its would-be-extrapolation to the $N = 0$ phase. Diamonds on the main panel and in the inset depict the coordinates of the $R(T)$ maxima at various fields.
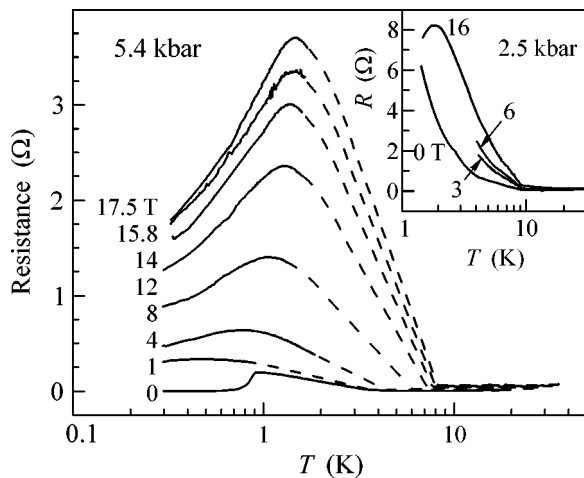
Fig. 2. Resistance R vs. temperature at pressure $P = 5.4$ kbar in the SDW regime for different fields. Data for $B = 0$ and 15.8 T were measured over the entire range of T (solid lines); for other fields, data were taken only at $T < 1.7$ K (solid lines). Dashed lines depict the anticipated behavior of $R(T)$. Inset shows similar results for $P = 2.5$ kbar.

phase with $N = 0$. On the other hand, these maxima in $R(T)$ follow a borderline $T_0(B)$, which has a fundamental meaning [7].

The aim of the current studies is (i) to test whether the above explanation holds and $R(T)$ becomes monotonic in the dielectric $N = 0$ phase and (ii) to verify whether or not the quantum/semiclassical borderline

$T_0(B)$ extends to the dielectric $N = 0$ phase as illustrated by the question mark in the inset to Fig. 1.

We found an unexpected behavior of the resistance in the $N = 0$ phase: as temperature decreases, the resistance does not increase monotonically as anticipated for the insulating SDW state but exhibits a maximum and falls further by a factor of ≥ 2. The scaling analysis of $R(T)$ for $N = 0$ and for the FISDW regime at $N \neq 0$ showed that the two effects of maxima in $R(T)$ have different critical exponents and thus the features of the resistance in the $N = 0$ and $N \neq 0$ phases have different origin. Our results demonstrate that the $T_0(B)$ boundary plotted through the high-order FISDW phases has no extension in the lowest order $N = 0$ phase; this is consistent with the current theoretical interpretation [9]. On the other hand, the unexpected $R(T)$ maximum in the purely insulating $N = 0$ phase has no explanation in the frameworks of the existing theories.

Measurements were carried out on two samples (of a typical size $2 \times 0.8 \times 0.3$ mm³) grown from a solution by a conventional electrochemical technique. We used either four ohmic contacts formed at the $a–b$ plane or eight contacts at two $a–c^*$ planes; in all cases 25-µm Pt wires were attached by a graphite paint to the sample along the most conducting direction a. The sample and a manganin pressure gauge were inserted into a Teflon cylinder placed inside a nonmagnetic 18-mm-o.d. pressure cell [11] filled with a Si-organic pressure transmitting liquid. The cell was mounted inside the liquid He⁴, or He³/He⁴, mixing chamber, in a bore of a superconducting magnet. For all measurements, the magnetic field was applied along z. The sample resistance was measured by a four-probe ac technique at 132 Hz, with a typical current of 1.5 µA. The out-of-phase component of the measured voltage was negligibly small, indicating ohmic contacts to the sample. The temperature was varied slowly, at a rate ≤ 0.1 K/min, in order to avoid deterioration in sample quality. The changes in the sample resistance were fully reproducible during the measurements including temperature sweeps; this indicated that the sample quality did not change. Measurements were done in magnetic fields up to 17.5 T and for temperatures down to 0.12 K.

According to the existing theory [12–15] and the known $P–B–T$ phase diagram [2, 16], the insulating $N = 0$ phase can be realized in two ways: either at high pressures/high fields, $P > 6$ kbar, $B > 18$ T (as shown in the inset to Fig. 1), or at low pressures/low fields, $P < 6$ kbar. In the latter case, the required magnetic field B_z can be much lower; it should only exceed 0.2 T in order to quench the superconducting state. In the current studies, we focused on the low pressure/low field regime.

Figure 2 shows the temperature dependence of the resistance in different fields, measured at pressure 5.4 kbar. Starting from high temperatures, $R(T)$ shows a typical metallic behavior. At temperature T_{SDW}, the sample resistance starts growing, indicating the onset

of the SDW state (with $N = 0$). Unexpectedly, in this purely insulating state, R exhibits a maximum at $T_{max} \approx$ 1 K and falls by a factor of 2. Similar behavior of $R(T)$ was observed also at $P = 2.5$ and 5.5 kbar (the results for $P = 2.5$ kbar are shown in the inset to Fig. 2). The maximum in $R(T)$ is seen for any magnetic fields; the temperature of the maximum increases with the field. By taking I–V curves in the vicinity of the T_{max}, we verified that the $R(T)$ maxima are not related to depinning or Joule heating.

The $R(T)$ maxima seem similar to the ones typical for the FISDW regime at $N \neq 0$ (shown in Fig. 1). However, the temperature of the $R(T)$ maximum, T_{max}, in the insulating $N = 0$ phase is less than that in the neighboring $N = 1$ phase by a factor of $\gtrsim 2$. This substantial difference cannot be due to the minor difference in pressure (7 kbar vs. 5.4 kbar) because T_{max} is only weakly pressure dependent [17]. It follows therefore that the measured T_{max} values in the $N = 0$ phase do not belong to the borderline $T_0(B)$ linearly extrapolated to the $N = 0$ phase (dashed line in the inset to Fig. 1). Since we did not observe other $R(T)$ maxima (i.e., at $T > T_{max}$) in the $N = 0$ phase, we conclude that the semiclassical/quantum borderline, $T_0(B)$, existing throughout the $N > 0$ FISDW phases does not extend to the insulating $N = 0$ phase.

The fundamentally different origin of the $R(T)$ maxima in the FISDW and SDW phases is demonstrated by the following scaling analysis of the corresponding $R(T)$ data. In this procedure, we normalized the resistance $R(T)$ (for all curves taken at different magnetic fields) by its maximum value $R_{max} = R(T_{max})$ and replaced the temperature T for each curve by the reduced temperature T/T_{max}. Figures 3a and 3b show the result of such simple scaling for $N = 0$ and $N \neq 0$ (i.e., for the SDW and FISDW regimes, respectively).

All the data (taken for different magnetic fields) collapse onto two different universal dependences $R(T/T_{max})/R(T_{max})$. For $N = 0$, all $R(T)$ curves measured at magnetic fields from 1 to 17.5 T scale excellently, thus demonstrating a similar origin. For $N > 0$ (Fig. 3b), the scaling is also good, though there is a minor systematic departure of the individual curves from the scaling curve, which increases with N. We emphasize that the two universal scaling curves in Figs. 3a and 3b are clearly different; the two scaling exponents $T_{max} \propto B^\gamma$ are also different, $\gamma = 1.5$ and 0.4, respectively (see the inset to Fig. 3). This difference demonstrates that the $R(T)$ maxima in the SDW phase and in the FISDW regime have different underlying mechanisms.

The borderline $T_0(B)$ determined empirically in [6] separates the regions of the existence and the absence of first-order phase transitions. It was also found that $R(T)$ for different fields and pressures exhibits a maximum at nearly the same border. On the other hand, according to the theory [8, 9], the maxima of $R(T)$ in the FISDW regime are caused by the developing QHE. Our
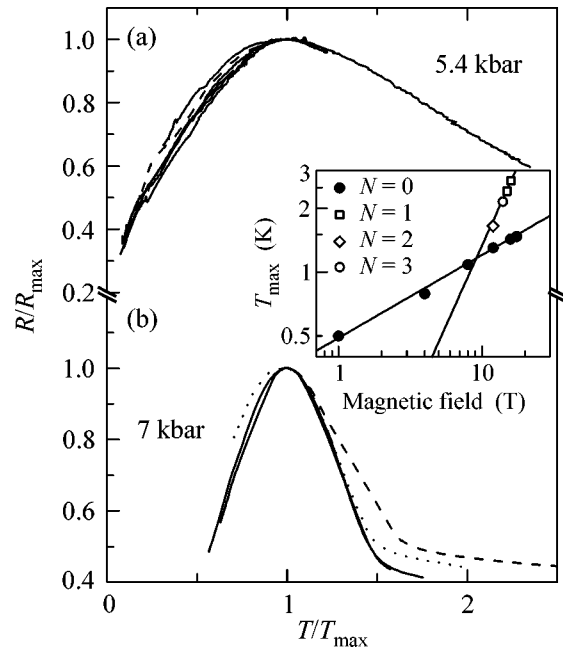
Fig. 3. Normalized resistance $R(T)$ versus normalized temperature for different fields: (a) for $P = 5.4$ kbar ($N = 0$) and (b) for $P = 7$ kbar and various $N \neq 0$ (data are calculated from Figs. 2 and 1, respectively). Inset shows T_{max} vs. magnetic field.

finding that the $T_0(B)$ borderline has no extension to the $N = 0$ phase is therefore in good agreement with the above interpretation, because there is no QHE in the $N = 0$ phase. Our data thus indicate that the QHE develops only in the "quantum" (low-T) domain. This conclusion suggests the absence of the QHE in the high-N phases where $T_0(B)$ vanishes to zero, e.g., for $N > 6$ at $P = 7$ kbar (see the inset to Fig. 1).

In the purely insulating $N = 0$ phase, the QHE is missing and the appearance of the $R(T)$ maxima cannot be explained by the growth of the off-diagonal conductivity. Therefore, the origin of the $R(T)$ maxima and of the strong drop in resistance towards low temperatures is puzzling. We wish to note an interesting coincidence. The temperature of the $R(T)$ maxima in the $N = 0$ phase is ≈ 1.5 K in strong magnetic fields ($B = 15$–17 T). On the other hand, the magnetoresistance in the $N = 0$ phase exhibits "rapid oscillations" [18] whose amplitude vanishes as T decreases below approximately the same temperature, 1.5 K. A symmetry-group analysis [19] shows that, in $(TMTSF)_2X$ compounds, there exist two incommensurate spin density waves. Although the second SDW has a smaller magnitude, it causes "rapid oscillations" and may preserve semimetallic properties as $T \longrightarrow 0$. It is noteworthy that the low-temperature region of the SDW phase diagram of $(TMTSF)_2PF_6$ was shown to have a nontrivial origin [20, 21] and was suggested to have an inner structure. We therefore cannot exclude that the above-described metallic-like behavior

of resistivity in the $N = 0$ phase is somewhat related to the inner subphases of the $N = 0$ SDW phase.

To summarize, we studied the temperature and magnetic field dependence of the resistance of the quasi-one-dimensional compound $(TMTSF)_2PF_6$ in both the FISDW ($N \neq 0$) and SDW ($N = 0$) phases. We found that the borderline $T_0(B, P)$ that divides the FISDW region of the P–B–T phase diagram into the hysteresis and nonhysteresis domains terminates in the $N = 1$ subphase; the border has no extension to the SDW $N = 0$ phase. The maxima of $R(T)$ in the FISDW region develop only in the $N \neq 0$ phase; their existence thus correlates with the existence of the QHE. This co-occurrence agrees with the current theoretical explanation of the $R(T)$ maxima in the $N \neq 0$ phases. We found that, in the SDW $N = 0$ phase, which is considered to be insulating, the resistance does not grow infinitely as temperature decreases but exhibits a maximum at $T_{max} \approx$ 1–2 K and falls at lower temperatures. We found that the temperature of the $R(T)$ maxima, $T_{max}(B)$, in the SDW phase is not a continuation of the borderline $T_0(B)$ which separates the hysteretic and nonhysteretic domains in the $N \neq 0$ regime. A scaling analysis of the resistance has shown that the $R(T)$ maxima in the $N = 0$ and $N \neq 0$ phases have a different origin. The unexpected strong drop of the resistance in the SDW $N = 0$ phase at $T < 1.5$ K has no explanation within the framework of existing theories.

REFERENCES

1. L. P. Gor'kov and A. G. Lebed, J. Phys. Lett. **45**, L-433 (1984); L. P. Gor'kov, Sov. Phys. Usp. **27**, 809 (1984).
2. P. M. Chaikin, J. Phys. I **6**, 1875 (1996).
3. K. Maki, Phys. Rev. B **33**, 4826 (1986); A. Virosztek, L. Chen, and K. Maki, Phys. Rev. B **34**, 3371 (1986).
4. S. T. Hannahs, J. S. Brooks, W. Kang, *et al.*, Phys. Rev. Lett. **63**, 1988 (1989).
5. J. R. Cooper, W. Kang, P. Auban, *et al.*, Phys. Rev. Lett. **63**, 1984 (1989).
6. A. V. Kornilov, V. M. Pudalov, Y. Kitaoka, *et al.*, Phys. Rev. B **65**, 060404(R) (2002).
7. A. G. Lebed, JETP Lett. **72**, 141 (2000).
8. W. Kang, S. T. Hannahs, L. Y. Chiang, *et al.*, Phys. Rev. B **45**, 13566 (1992).
9. V. M. Yakovenko and H.-S. Goan, Phys. Rev. B **58**, 10648 (1998).
10. T. Vuletić, C. Pasquier, P. Auban-Senzier, *et al.*, Eur. Phys. J. B **21**, 53 (2001).
11. A. V. Kornilov, V. A. Sukhoparov, and V. M. Pudalov, *High Pressure Science and Technology*, Ed. by W. Trzeciakowski (World Sci., Singapore, 1996), p. 63.
12. M. Heritier, G. Montambaux, and P. Lederer, J. Phys. Lett. **45**, L-943 (1984).
13. A. G. Lebed, Sov. Phys. JETP **62**, 595 (1985).
14. K. Maki, Phys. Rev. B **33**, 4826 (1986).
15. K. Yamaji, Synth. Met. **13**, 29 (1986).
16. W. Kang, S. T. Hannahs, and P. M. Chaikin, Phys. Rev. Lett. **70**, 3091 (1993).
17. Figure 2 shows that the T_{max}-values measured at $P = 2.5$ and 5.4 kbar differ from each other less than by 20%.
18. J. P. Ulmet, L. Bachere, and S. Askenazy, Solid State Commun. **58**, 753 (1986); S. Uji, J. S. Brooks, M. Chaparala, *et al.*, Phys. Rev. B **55**, 12446 (1997).
19. A. G. Lebed, Phys. Scr. **39**, 386 (1991).
20. T. Takahashi, T. Harada, Y. Kobajashi, *et al.*, Synth. Met. **41–43**, 3985 (1991).
21. J. C. Lasjaunias, K. Biljaković, F. Nad', *et al.*, Phys. Rev. Lett. **72**, 1283 (1994).

Entanglement Fidelity of Coherent-State Teleportation with Asymmetric Quantum Channel[¶]

A. V. Chizhov

Bogoliubov Laboratory of Theoretical Physics, Joint Institute for Nuclear Research,
Dubna, Moscow region, 141980 Russia

Received October 21, 2004

A strategy for teleporting coherent states with the entanglement fidelity is considered in the general case of an asymmetric teleportation scheme. It is shown that the nonbalanced homodyne detection with the subsequent coherent displacement is required to provide the average teleportation fidelity of entanglement. © *2004 MAIK "Nauka/Interperiodica"*.

PACS numbers: 03.65.–w; 03.67.–a; 42.50.Dv

1. INTRODUCTION

Quantum teleportation is now considered to be a key method for transmission of quantum states in communication protocols, among which quantum teleportation of continuous variables is of great importance [1–3]. An essential point of quantum teleportation lies in a quantum channel between the sending and receiving stations, which is provided by a bipartite entangled state. In the case of continuous-variable quantum teleportation, a two-mode squeezed vacuum state (TMSV) serves as the source of entanglement. The degree of entanglement is then controlled by the degree of squeezing, so that faithful teleportation requires a source of rather strong squeezing. Since the generation of highly squeezed states is quite an arduous problem, some improved protocols were proposed to maximize the quality of teleportation at finite squeezing [4–6]. In reality, however, because of unavoidable environmental influences, a TMSV turns into a mixed state that leads to further degradation of the initial entanglement and thus makes teleportation still worse. The consideration of continuous-variable quantum teleportation in noisy channels was the subject of a number of papers. In particular, schemes for increasing the degree of entanglement by purification were suggested [7, 8] and the influence of the thermal bath on propagation of the entangled modes was analyzed [9–11].

The criterion that displays the efficiency of teleportation is its average fidelity. However, in general, such a fidelity does not directly reveal the preserved amount of entanglement in the quantum channel and thus cannot serve as a sensitive measure of teleportation. For this, the *entanglement* fidelity is required [12]. The entanglement fidelity was shown to equal the standard fidelity of teleportation of pure states in the case of the symmetric Gaussian channel and was first obtained by Braunstein and Kimble [2]. Their teleportation protocol was based on balanced homodyne detection in the sending station and proper coherent displacement in the receiving station. As to teleportation with an asymmetric quantum channel, in the framework of the given protocol, such an equivalence between the fidelities is no longer true, since teleportation becomes dependent on transmitting states [11].

This letter is aimed at demonstrating the possibility of realizing teleportation with the entanglement fidelity for asymmetric teleportation schemes. As the teleporting states, coherent states are assumed to be taken, which play a significant role in optical communication. In this way, nonbalanced homodyne detection is to be applied in the sending station depending on the propagation paths of the modes from the source of entanglement, which, in turn, completely determines the corresponding displacement operation in the receiving station.
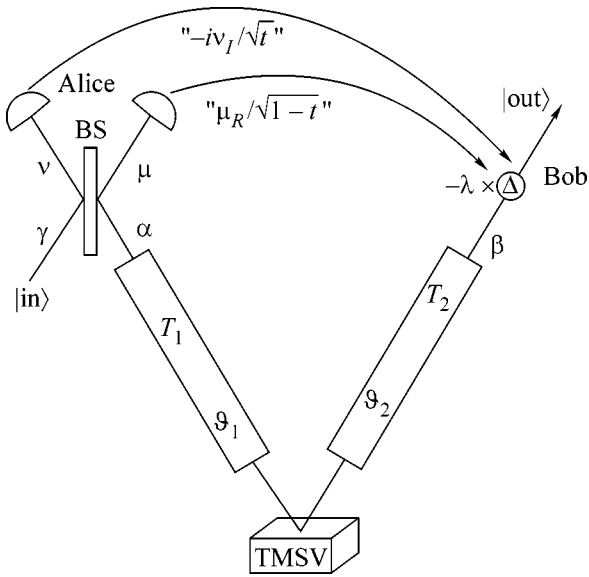
2. THE TELEPORTATION SCHEME

Let us consider the scheme of continuous-variable single-mode teleportation sketched in Fig. 1. In this scheme, TMSV is used as the source of entanglement. Assume that the initially squeezed modes (with the squeezing parameter $\zeta = |\zeta|e^{i\varphi}$) propagate to the sending station (Alice) and to the receiving station (Bob) through the paths having the transmission coefficients T_1 and T_2 and embedded in the thermal baths at temperatures ϑ_1 and ϑ_2, respectively. Then the resulting state will be described by the following Wigner function [13]:

$$W^{\mathrm{E}}(\alpha, \beta) = \frac{4}{\pi^2 \mathcal{N}}$$

$$\times \exp[-2(C_2|\alpha|^2 + C_1|\beta|^2 + S^*\alpha\beta + S\alpha^*\beta^*)],$$

(1)

Fig. 1. The teleportation scheme for transmitting quantum states from Alice to Bob. In quotes is shown information that Alice sends to Bob using the classical channel after her nonbalanced homodyne measurements by the beam splitter of transmissivity t.

where $(i = 1, 2)$

$$S = \frac{e^{i\varphi}}{\mathcal{N}} T_1 T_2 \sinh 2|\zeta|, \tag{2}$$

$$C_i = \frac{1}{\mathcal{N}}[1 + |T_i|^2(\cosh 2|\zeta| - 1) + 2n_{\text{th}\,i}(1 - |T_i|^2)], \tag{3}$$

$$\mathcal{N} = [1 + |T_1|^2(\cosh 2|\zeta| - 1) + 2n_{\text{th}\,1}(1 - |T_1|^2)]$$
$$\times [1 + |T_2|^2(\cosh 2|\zeta| - 1) + 2n_{\text{th}\,2}(1 - |T_2|^2)] \tag{4}$$
$$- |T_1 T_2|^2 \sinh^2 2|\zeta|,$$

with $n_{\text{th}\,i} = \{\exp[\hbar\omega/(k_B \vartheta_i)] - 1\}^{-1}$ being the corresponding mean numbers of thermal excitations. The Gaussian form of the Wigner function (1) makes it possible to estimate analytically the residual amount of entanglement that can still be preserved in the (mixed) state shared by Alice and Bob. According to [14], the measure of entanglement is determined by the expression

$$E = -\frac{1}{2}\log_2\left\{\frac{\mathcal{N}^2}{2}[C_1^2 + C_2^2 + 2|S|^2 \right.$$
$$\left. - (C_1 + C_2)\sqrt{(C_1 - C_2)^2 + 4|S|^2}]\right\}, \tag{5}$$

when E takes on positive values, and is zero otherwise, i.e., when the state appears to become separable (see [15]). In the particular case of symmetric paths of mode

propagation $(C_1 = C_2 \equiv C)$, expression (5) is simplified to

$$E = -\log_2 \mathcal{N}(C - |S|). \tag{6}$$

In order to make use of the available quantum channel for teleporting an input quantum state, Alice performs a homodyne measurement on this mode and the mode being disposed at the sending station from the source by combining them through a (lossless) beam splitter. It is worth noting here that the beam splitter is presumed not to be the obligatory 50 : 50% one, unlike what is implied in the standard approach, but having some arbitrary transmissivity t. A similar scheme was used in [6] for maximizing the teleportation fidelity. If $W_{\text{in}}(\gamma)$ is the Wigner function of the input state, then as a result of such a combination one obtains the Wigner function of the (three-mode) overall system to be

$$W_S(\mu, \nu, \beta)$$
$$= W_{\text{in}}(\mu\sqrt{t} - \nu\sqrt{1-t}) W^E(\mu\sqrt{1-t} + \nu\sqrt{t}, \beta). \tag{7}$$

When the measurement of the real part of μ, μ_R, and the imaginary part of ν, ν_I, is made, Bob's mode will be found in a quantum state, whose Wigner function is given by

$$W_B(\beta|\mu_R, \nu_I) = \frac{4}{\pi^2 \mathcal{N}\sqrt{t(1-t)}}\exp\left[-\frac{2}{C_2\mathcal{N}}|\beta|^2\right]$$
$$\times \iint d\gamma_R d\gamma_I W_{\text{in}}(\gamma_R + i\gamma_I)\exp\left[-2C_2\left|\left(\frac{\mu_R}{\sqrt{1-t}} - i\frac{\nu_I}{\sqrt{t}}\right)\right.\right. \tag{8}$$
$$\left.\left. + \frac{S^*}{C_2}\beta - \left(\gamma_R\sqrt{\frac{t}{1-t}} + i\gamma_I\sqrt{\frac{1-t}{t}}\right)\right|^2\right].$$

Then, relying upon the pair of Alice's measurement data μ_R and ν_I at the fixed transmissivity t of the beam splitter that enter Eq. (8) in the form of

$$\Delta(\mu_R, \nu_I) \equiv \mu_R/\sqrt{1-t} - i\nu_I/\sqrt{t}, \tag{9}$$

Bob may coherently displace the quantum state of his mode by applying the displacement $\beta \longrightarrow \beta - \lambda\Delta(\mu_R, \nu_I)$ with some arbitrary strength λ. Thus, after averaging over all the measurement outcomes, it will create the teleported quantum state on average:

$$W_{\text{out}}(\beta) = \iint d\mu_R d\nu_I W_B(\beta - \lambda\Delta(\mu_R, \nu_I)|\mu_R, \nu_I). \tag{10}$$

As a criterion of teleportation, one can use the fidelity of the final state (10) to the initial one, which in the case of a pure input state is given by the overlap of their Wigner functions

$$F = \pi\iint d^2\beta W_{\text{in}}(\beta) W_{\text{out}}(\beta). \tag{11}$$

This fidelity is evidently dependent on the teleportation protocol as a whole and so can only optionally display the character of the quantum channel. Taking as an

example the teleportation of coherent states, it will be shown how the fidelity (11) can be turned into the fidelity of entanglement for the general case of the asymmetric quantum channel.

3. TELEPORTATION OF COHERENT STATES

Now apply the teleportation scheme from the preceding section for transmitting coherent states. Performing all steps of the teleportation protocol, such as homodyne detection with the beam splitter of transmissivity t and the coherent displacement of the strength λ, after straightforward calculations, one can arrive at the following expression for the fidelity of teleportation of the coherent state $|\alpha_0\rangle$:

$$F_{coh}(\alpha_0)$$

$$= \frac{2\exp\left\{-\dfrac{2(\sqrt{1-t}-\lambda\sqrt{t})^2}{1-t+\lambda^2 t+(1-t)\sigma(\lambda)}\alpha_0^2\right\}}{\sqrt{\left[\sigma(\lambda)+\lambda^2\dfrac{t}{1-t}+1\right]\left[\sigma(\lambda)+\lambda^2\dfrac{1-t}{t}+1\right]}}, \quad (12)$$

where $\sigma(\lambda) = \mathcal{N}(C_2 + \lambda^2 C_1 - 2\lambda|S|)$. This fidelity is a generalization of the analogous expression obtained in [11] for the case of balanced homodyning, i.e., when $t = 0.5$. At large α_0, the fidelity (12) is seen to have an exponential suppression factor unless

$$\lambda = \sqrt{\frac{1}{t} - 1}, \quad (13)$$

at which the dependence on the coherent amplitude entirely disappears, so that the fidelity has the form

$$F_{coh} = \frac{2}{\sqrt{[\sigma(\lambda)+2][\sigma(\lambda)+\lambda^4+1]}}. \quad (14)$$

For the symmetric quantum channel, when balanced homodyning, $t = 0.5$, is to be used, the choice of the strength of the coherent displacement $\lambda = 1$ satisfies the suppression condition (13) and leads the fidelity (14) to the form

$$F_{coh}^{sym} = \frac{2}{2+\sigma^{sym}(1)} = \frac{1}{1+\mathcal{N}(C-|S|)}. \quad (15)$$

Taking into account relation (6), one can see that the fidelity (15) is nothing but the entanglement fidelity of teleportation

$$F_{coh}^{E} = \frac{1}{1+2^{-E}}. \quad (16)$$

For the entangled teleportation channel, $E > 0$, this fidelity lies above 0.5, approaching unity for infinite entanglement (the case of perfect teleportation). Thus, the value 0.5, corresponding to $E = 0$, can be considered as the classical limit of teleportation, below which entanglement in the quantum channel is absent.
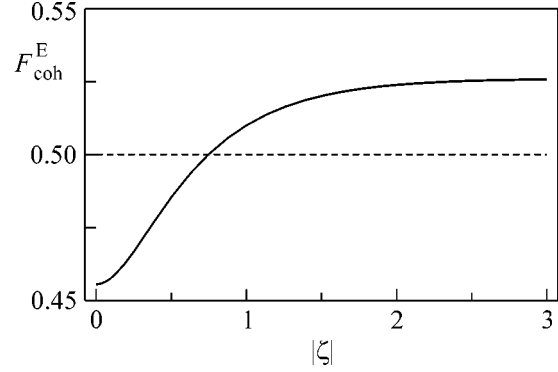
Fig. 2. The entanglement fidelity (16) of coherent-state teleportation is shown as a function of $|\zeta|$ at $|T_1| = 0.95$, $|T_2| = 0.85$ and $n_{th\,1} = 1$, $n_{th\,2} = 2$ in accordance with the definition (5).

However, to assure the entanglement fidelity (16) in an asymmetric case, balanced homodyning turns out to be unacceptable. Indeed, even if λ, according to Eq. (13), is chosen to equal 1 to eliminate the suppression factor, anyway the fidelity (12) can be below the classical limit 0.5 at the entangled teleportation channel. It is due to the asymptotic behavior of σ at the large squeezing parameter $|\zeta|$,

$$\sigma(\lambda) \simeq \frac{1}{2}(|T_2| - \lambda|T_1|)^2 e^{|2\zeta|} \quad (17)$$

which disperses at $\lambda = 1$ for $|T_1| \neq |T_2|$. Thus, the fidelity of teleportation in such a case

$$F_{coh} = \frac{2}{2+\sigma(1)} \simeq \frac{1}{1+\dfrac{1}{4}(|T_2|-|T_1|)^2 e^{|2\zeta|}}$$

diminishes to zero at large initial squeezing regardless of the entanglement increase.

The way to obtain the entanglement fidelity in an asymmetric teleportation scheme can be found by means of nonbalanced homodyning. The transmissivity t of the beam splitter is then no longer fixed at 0.5, but must be determined with the help of relation (13) by adjustment of the coherent displacement strength λ to fulfill the equivalence between the fidelities (14) and (16). The result of such fitting will be varied depending on the specific conditions of the mode propagation and source squeezing. The choice of t will also fix the base Δ of the coherent displacement in Eq. (9), so that all steps of the teleportation strategy to provide the fidelity of entanglement become completely definite.

An example demonstrating how this procedure can be done for the particular case of mode propagation is illustrated in Figs. 2 and 3. The behavior of the entanglement fidelity as a function of the source squeezing is shown in Fig. 2. The fidelity is seen to exceed the classical limit of 0.5 starting only from $|\zeta| \approx 0.75$, which indicates the absence of entanglement between the
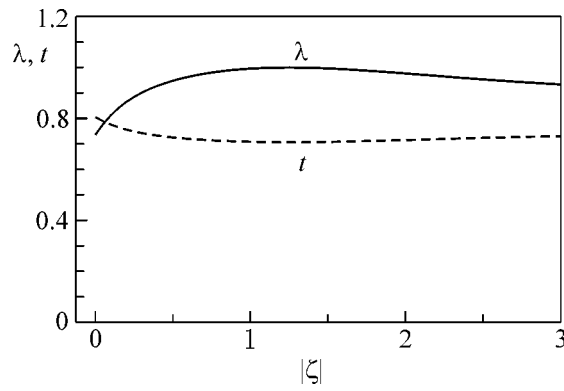
Fig. 3. The strength λ of the coherent displacement (solid line) and, according to Eq. (13), the transmissivity t of the beam splitter (dotted line), which provide coherent-state teleportation with the entanglement fidelity, are shown as a function of $|\zeta|$ at the same propagation parameters as in Fig. 2.

modes in Alice's and Bob's hands at a squeezing parameter of the source below this value. It means that, for $|\zeta| < 0.75$, the corresponding initial entanglement between the modes, provoked by the squeezing, is entirely wasted because of absorption losses in their propagation from the source. The proper choices of the strength λ of the coherent displacement and the transmissivity t as the result of computer adjustment to provide this entanglement fidelity of teleportation are plotted in Fig. 3. It can be seen that, at large $|\zeta|$, the strength λ tends to $|T_2|/|T_1| \approx 0.9$, which protects σ from dispersion in accordance with Eq. (17).

4. CONCLUSIONS

A teleportation scheme with the mixed quantum channel has been analyzed from the point of view of realizing the transmission of coherent states with the entanglement fidelity. The mixed teleportation channel is associated with absorption losses in the transmission of the TMSV modes along the paths to the sending and receiving stations.

It has been shown that the entanglement fidelity of teleportation with the asymmetric quantum channel could be achieved by means of Bob's specific coherent displacement relying on results of Alice's nonbalanced homodyne measurement. However, in order to match the necessary transmissivity of the measurement beam splitter and the corresponding parameters of the displacement, one needs to know information on the initial squeezing in the source as well as the conditions of the mode propagation. This fact fundamentally distinguishes the case of the asymmetric quantum channel from the symmetric one, when teleportation with the entanglement fidelity occurs at fixed parameters independent of the scheme.

REFERENCES

1. L. Vaidman, Phys. Rev. A **49**, 1473 (1994).
2. S. L. Braunstein and H. J. Kimble, Phys. Rev. Lett. **80**, 869 (1998).
3. T. C. Ralph and P. K. Lam, Phys. Rev. Lett. **81**, 5668 (1998).
4. T. Opatrný, G. Kurizki, and D.-G. Welsch, Phys. Rev. A **61**, 032302 (2000).
5. T. Ide, H. F. Hofmann, A. Furusawa, and T. Kobayashi, Phys. Rev. A **65**, 062303 (2002).
6. P. T. Cochrane and T. C. Ralph, Phys. Rev. A **67**, 022313 (2003).
7. L.-M. Duan, G. Giedke, J. I. Cirac, and P. Zoller, Phys. Rev. Lett. **84**, 4002 (2000).
8. S. Parker, S. Bose, and M. B. Plenio, Phys. Rev. A **61**, 032305 (2000).
9. J. Lee, M. S. Kim, and H. Jeong, Phys. Rev. A **62**, 032305 (2000).
10. M. Ban, M. Sasaki, and M. Takeoka, J. Phys. A: Math. Gen. **35**, L401 (2002).
11. A. V. Chizhov, L. Knöll, and D.-G. Welsch, Phys. Rev. A **65**, 022310 (2002).
12. B. Schumacher and M. Nielsen, Phys. Rev. A **54**, 2629 (1996).
13. A. V. Chizhov, E. Schmidt, L. Knöll, and D.-G. Welsch, J. Opt. B: Quantum Semiclass. Opt. **3**, 77 (2001).
14. G. Vidal and R. F. Werner, Phys. Rev. A **65**, 032314 (2002).
15. R. Simon, Phys. Rev. Lett. **84**, 2726 (2000).